

POLITECNICO DI TORINO

Corso di Laurea Magistrale in Ingegneria Aerospaziale



Tesi di Laurea Magistrale

Evaluating RANS capabilities to simulate lean blowout of a gaseous fuel flame in a model combustion chamber

Relatori

Prof. F. Larocca

Prof. I. Zubrilin

Candidato

Guido Mazza

Aprile 2021

Summary

Modern gas turbine engine's emissions are strictly regulated nowadays, in order to have the lowest possible impact on the environment. These restrictions led to changes in the design process of the combustor, to achieve and maintain high reliability and performances. Before the introduction of these restrictions, diffused combustion was used in the combustion chamber. It resulted in low pressure losses, high efficiency and performances provided by the engine. Now Lean Premixed and Prevaporized flow (LPP) is mostly used in modern combustors. However, this technology brings two main problems: combustion instabilities and flame extinction. Due to the proximity to the flame quenching, Lean Blowout (LBO) has been studied over the past years and because of the high cost and difficulties of its experimental tests, many empirical relations and numerical methods have been born in the last decades to predict it. Numerical methods include CFD calculations using RANS or LES. The purpose of this work is to demonstrate the capabilities of RANS models to simulate Lean Blowout of a gaseous fuel flame. Some user defined functions(UDF) are also proposed and used in this work to simulate flame extinction closer to reality. Numerical results will be compared with some experimental data collected in the Samara National Research University's Laboratory, where a reference combustor has been tested for different operating conditions.

Acknowledgements

Among all others, I would like to first thank my family. Especially my parents, Maurizio e Licia for all the sacrifices they've done in the last years for my studies and for never stopping motivating me. A special mention goes to my sister, Alessia, for always believing in me and for being an academic inspiration.

My sincere gratitude goes to both my supervisors, Professor Larocca and Professor Zubrilin, for making this work possible. I was honored to work with such professional and competent figures.

Thanks to Ceci, for being a wonderful reference point, with her unconditional love and support, especially during hard times.

I would also like to thank prof. Vinogradov and all the people related to my russian experience: Nicolas, Antonino, Beatrice, Adriana and all the Aegee members. Thanks for welcoming us so warmly and for all the experiences together.

A special thanks to my closest friends in Latina, and to the ones in Torino: Tommaso, Alessandro, Alberto, Anna and all the others from Collegio Einaudi. For all the wonderful emotions and experiences shared in the last years.

In the end, a special mention goes to my classmates at Politecnico: Salvatore, Leonardo, Marina, Andrea, Raimondo, Luca e Alessandro. For all the laughs and the difficulties lived together during these years.

To them, but also to all the others, I sincerely wish good health and a life full of success.

Table of Contents

List of Tables	VII
List of Figures	VIII
1 Blowout phenomenon	1
1.1 The issue with emissions	1
1.1.1 NO_x emissions in gas turbine engines	2
1.1.2 Reducing emissions - LPP Technology	2
1.1.3 Research motivation	3
1.2 Background on LBO analysis	3
1.2.1 First approaches in LBO prediction	3
1.2.2 Numerical methods - CFD simulations	5
1.2.3 Hybrid methods	7
1.2.4 The role of CFD in models validation	8
1.2.5 Purpose of this work	9
2 Modeling turbulence and combustion	10
2.1 Turbulence modeling	10
2.1.1 Definition of turbulence	10
2.1.2 Energy spectrum of turbulence	11
2.1.3 Governing equations	12
2.1.4 Navier-Stokes equations	20
2.2 Reynolds averaged Navier-Stokes equations (RANS)	20
2.2.1 Mixing length model	23
2.2.2 Standard $k - \epsilon$ model	24
2.2.3 Realizable $k - \epsilon$ model	26
2.2.4 Reynolds stress model (RSM)	29
2.2.5 URANS formulation	33
2.3 Combustion modeling	34
2.3.1 Combustion regimes	35
2.3.2 Flamelet Generated Manifold (FGM)	36

2.3.3	Species and reactions	41
2.4	User defined Functions	41
2.4.1	Laminar flame speed	41
2.4.2	Critical strain rate	47
3	Numerical and experimental setup	52
3.1	Description of the combustion chamber	52
3.2	Mesh	53
3.3	Boundary conditions	54
3.3.1	Inlet	54
3.3.2	Outlet	55
3.3.3	Pilot fuel and Main fuel	55
3.4	Solution monitors set	57
3.5	Running the simulations	59
3.6	Experimental setup	60
4	Results	62
4.1	Numerical results	62
4.1.1	Realizable $k - \epsilon$ model	65
4.1.2	Reynolds Stress Model	71
4.1.3	Realizable $k - \epsilon$ with UDF	75
4.1.4	URANS	79
4.2	Experimental results	83
5	Conclusions	85
5.1	Future developments	86
A	Appendix	88
	Bibliography	91

List of Tables

1.1	Previous works on LBO investigation	7
2.1	Model constants - Standard $k - \epsilon$ [30]	25
2.2	Model constants - Realizable $k - \epsilon$ model [31]	28
2.3	Model constants - RSM[39]	32
2.4	Species employed in the combustion model	41
2.5	Coefficients of eq.(2.59) [51]	43
2.6	Coefficients of equations (2.62, 2.63)	44
3.1	Fuel distribution in tested cases	57
3.2	Fuel values for Point 2	58

List of Figures

1.1	Variation of fuel mass flow rate and temperature in Piehl's work[8]	6
2.1	Kinetic energy spectrum [15]	11
2.2	Fluid element	13
2.3	Mass fluxes	13
2.4	Stresses on fluid element	15
2.5	Stress balance for x-axis	15
2.6	Heat flux in a fluid element	18
2.7	Time averaging of a steady flow[25]	22
2.8	Ensemble averaging of an unsteady flow[25]	34
2.9	Different flame types of Bunsen burner [43]	36
2.10	Probability Density Function (PDF)	40
2.11	Visualization of laminar flame speed[50]	42
2.12	Laminar flame speed with $T_u = 800K$ and $P_u = 101325Pa$	45
2.13	Laminar flame speed's dependence on pressure, temperature and φ	45
3.1	Combustion chamber	53
3.2	Mesh visualization	54
3.3	Mesh section	55
3.4	Fuel inlets	56
3.5	Fuel lowering method for Point 2	57
3.6	Burner	61
3.7	Experimental setup	61
4.1	Inlet flow streamlines	63
4.2	Streamlines for main and pilot fuel	64
4.3	Contour of static temperature at stable combustion and near LBO	66
4.4	Contour of velocity at stable combustion and near LBO	67
4.5	Contour of progress variable at stable combustion and near LBO	68
4.6	Temperature and Progress variable evolution during simulation	69
4.7	Lean Blowout results for Realizable $k - \epsilon$ model without UDF	70

4.8	Contour of Temperature - $\alpha = 5.05$ - Point 3	71
4.9	Contour of progress variable - $\alpha = 5.05$ - Point 3	72
4.10	Temperature and Progress variable evolution during simulation . . .	73
4.11	Lean Blowout results for Reynolds Stress Model without UDF . . .	74
4.12	Contour of Temperature - $\alpha = 4.55$ - Point 2	75
4.13	Contour of Progress variable - $\alpha = 4.55$ - Point 2	76
4.14	Temperature and Progress variable evolution during simulation . . .	77
4.15	Lean Blowout results for Realizable $k - \epsilon$ model with UDF	78
4.16	Contour of Temperature - $\alpha = 2.85$ - Point 2	78
4.17	Contour of Progress variable - $\alpha = 2.85$ - Point 2	79
4.18	Contour of Temperature - $\alpha = 4.25$ - Point 2	80
4.19	Contour of Progress variable - $\alpha = 4.25$ - Point 2	80
4.20	Temperature and Progress variable evolution during simulation . . .	81
4.21	Lean Blowout results for URANS Realizable $k - \epsilon$ model without UDF	82
4.22	Comparison with experimental data - Diffusive Flamelets	83
4.23	Comparison with experimental data - Premixed Flamelets	84

Chapter 1

Blowout phenomenon

The aim of this chapter is to introduce the lean blowout phenomenon, object of this work. Its importance is introduced, as well as why concern about this phenomenon raised lately and why it is still studied and analyzed nowadays.

1.1 The issue with emissions

In the last decades, awareness and concern about pollutant emissions has increased in people and regulatory agencies. Power generation utilities, as the ones in aviation or in power plants, have witnessed wide changes in both regulations and technologies in order to reduce pollutant emissions. The main focus of many studies and recent regulations is to reduce pollutant emissions of all kind of gas-turbine engines. In September 2020 the European Union, as part of the European Green Deal, proposed to cut down at least 40% of greenhouse gas emission and to improve energy efficiency by 32.5% by 2030 (compared to 1990 levels)[1]. This is only one of many measures that governments and regulatory agencies are taking into account.

1.1.1 NO_x emissions in gas turbine engines

Gas turbine engines, used in both aviation and power generation, are a large source of pollutants. There are many exhaust products from a gas turbine engine. For example carbon dioxide CO_2 or monoxide CO , water vapor H_2O , unburned hydrocarbons UHC and nitrogen oxides NO_x . Although CO_2 and H_2O are not officially classified as pollutant, they strongly contribute to global warming and the only way to reduce their emission is burning less fuel. On the other side, NO_x emissions have been generating a lot of concern the last decades because these gaseous products can seriously damage plant lives as well as generating acid rains and affecting the ozone layer. In 2011 the European Environment Agency (EEA) stated that 41% of all NO_x emissions are from road transports, while 23% are from the energy production sector[2]. This puts enormous pressure on engine manufacturers, who have to find innovative technical solutions to this problem.

1.1.2 Reducing emissions - LPP Technology

Reducing pollutant emissions is the main goal of many engineering and regulatory choices. In order to reduce these harmful emissions, fuel consumption is being limited, thus the combustion regime has shifted over the years from rich mixtures to lean ones.

Nowadays, many combustors exploit the technology of LPP combustion, which stands for Lean Premixed and Prevaporized combustion. However, the use of this technology and the continuous seek for more efficient engines have led to other kinds of problems. In fact, it has been widely shown that although LPP combustion strongly reduces pollutant emissions, it suffers from 2 great problems: **reduced combustion stability** and **lean blowout** phenomenon. The ability for the combustor to always maintain a stable regime, in response to perturbations or different operating conditions, is one of the most important requirements to meet.

1.1.3 Research motivation

LPP combustion processes still remain an open research field, as literature is getting riper year by year. Moreover, a particular combustor configuration is analyzed in this work: a diffusive pilot flame with a premixed main flame. As explained in the next sections, there is a lack in literature on validation of this type of architecture, and more room is available for improvements.

1.2 Background on LBO analysis

Lean Blowout phenomenon(LBO) has been studied over the past years and because of the high cost and difficulties of its experimental tests, many numerical methods and empirical relations have been born in the last decades to predict it. One of the first empirical approach was proposed by A. H. Lefebvre[3] in 1985 but with higher modern requirements for combustion chambers made this approach less and less accurate over the years. Newer methods, as the one from Wang Z.[4], try to predict LBO starting from Lefebvre's relation and improving its accuracy using the Damkohler's number and defining a Practical Reaction Zone(PRZ). Numerical methods include CFD calculations using RANS or LES and over the years literature was enriched with contents involving numerical simulations.

1.2.1 First approaches in LBO prediction

A. H. Lefebvre[3] proposed a first empirical approach to predict lean blowout in 1985. He started his analysis with homogeneous mixture, stating that lean blowout fuel/air ratio q_{LBO} depends on the inlet air velocity, pressure, and temperature, and on the size of the combustion zone as follows:

$$q_{LBO} \propto \left[\frac{\dot{m}_A}{V P_3^n \exp(T_3/b)} \right]^x \quad (1.1)$$

where \dot{m}_A is the mass flow rate of the mixture, V is the combustion volume, P_3 and T_3 are the inlet pressure and temperature, n is the reaction order, b and x are two constants to be experimentally determined. Lefebvre also stated that it's possible to take into account heterogeneous mixtures with a coefficient combined with equation (1.1). In particular, for an heterogeneous mixture, if the fraction of fuel vaporized f_f can be calculated or is known, then:

$$q_{LBO(heterogeneous)} = q_{LBO(homogeneous)} x f_f^{-1} \quad (1.2)$$

after some reformulations and some considerations and correction with experimental data, Lefebvre exposed the first empirical relation to predict lean blowout[3]:

$$q_{LBO} = \left(\frac{A'' f_{pz}}{V_{pz}} \right) \left(\frac{\dot{m}_A}{P_3^{1.3} \exp(T_3/300)} \right) \left(\frac{D_0^2}{\lambda_{eff} LCV} \right) \quad (1.3)$$

where V_{pz} is the primary zone volume, A'' is an experimentally determined constant which depends on geometry and mixing characteristics, D_0 is the initial size of sprayed droplets, λ_{eff} is the effective value of evaporation constant, LCV is the lower calorific value of fuel. The first term of equation (1.3) is a function of the combustor design, the second term contains the operating conditions and the last one carries the influence of fuel properties.

Some improvements

Lefebvre's equation for lean blowout was widely used to predict this phenomenon quickly. However, after a closer look at equation (1.3) it's possible to notice that V_{pz} , which is the primary zone volume, or the volume ahead of dilution holes, is the only combustor configuration parameter contained in that equation. This means that, fixing all other parameters, different combustors with same V_{pz} will have the same LBO fuel/air ratio. And that of course it is questionable and requires further studies.

The study from Xie *et al.*[5] focused right on that. Thanks to experimental validation, they improved Lefebvre’s relation for lean blowout as follows:

$$q_{LBO} = K \left[\frac{\alpha}{\sqrt{\beta} + (1 - \alpha)\sqrt{\beta}} \right] \left(\frac{1}{V_{pz}} \right) \left(\frac{\dot{m}_A}{P_3^{1.3} \exp(T_3/300)} \right) \left(\frac{D_0^2}{\lambda_{eff} LCV} \right) \quad (1.4)$$

where K is an universal constant experimentally determined, α is the fraction of dome airflow and $\beta = \frac{V_f}{V_c}$ is the non dimensional flame volume.

1.2.2 Numerical methods - CFD simulations

In recent years, with the development of new combustors with different geometries, requirements and operating conditions, empirical relations like (1.3) cannot meet the design requirements of combustors. In fact, according to Hu *et al.*, Lefebvre’s relation for blowout prediction can reach an error of $\pm 50\%$ [6] and this is mainly attributed to poor flow physics modeling in the primary combustion zone. Thanks to numerous improvements in CFD modeling, and the great accessibility that this tool has seen lately, numerical investigations on lean blowout have been widely conducted, especially using steady or unsteady RANS or LES.

For example, the work from Akhtar *et al.*[7] is focused on that. They assessed the suitability of RANS equations in predicting lean blowout phenomenon. To do that they investigated the use of different mesh, turbulence models and combustion models, as well as tuning some parameters in the combustion model to make it closer to reality.

A good validation method has been conducted by Piehl *et al.* in 2018[8]. Their work was focused on validating Large Eddy Simulation (LES) and Adaptive Mesh Refinement (AMR) as effective tool for LBO prediction. They investigated two different fuels, a Jet-A fuel (CAT A2) and an alternative fuel (CAT C1). Their approach was very similar to the one used in this work. As a matter of fact, their strategy for LBO catching was divided in 2 phases:

- Flame stabilization performing several iterations;

- Reduction of fuel mass flow rate with a constant equivalence ratio step.

Outlet temperature was monitored looking for a drop that would indicate LBO. The graph in Figure (1.1) better shows their strategy to catch lean blowout and the drop of temperature that occurred for both fuels.

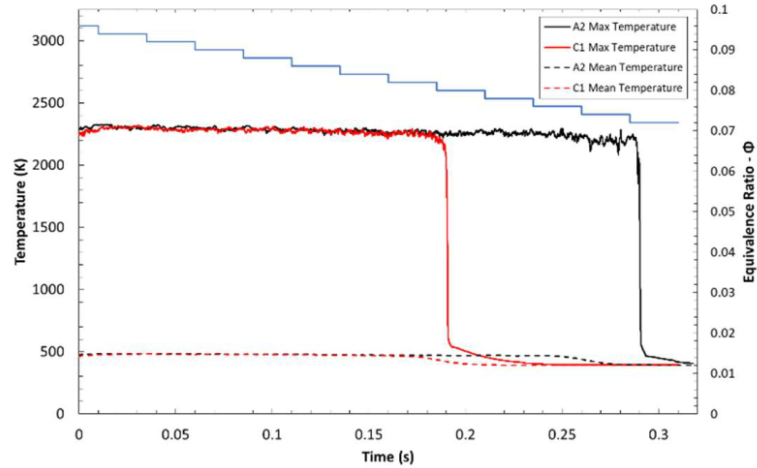


Figure 1.1: Variation of fuel mass flow rate and temperature in Piehl's work[8]

In the end, thanks to experimental data, they assessed LES as a good method for LBO prediction, as they found only a 9% discrepancy between simulations and experiments.

Another similar work was performed by Escaplez *et al.*[9]. They investigated LES sensitivity to LBO, changing fuel properties and lowering fuel mass flow rate. They found no major difference in the behaviour of the two fuels during blowout. These results are consistent with some experimental data they previously gathered. This way, LES approach was once again validated to investigate LBO for different fuels. A lot of effort was put in validating different combustion models too. A clear example of that is the work carried out by Ma *et al.*[10]. Two different combustion models were put to the test: a flamelet/progress variable one (FPV) and a thickened flame approach with finite-rate chemistry (TFLES). Comparing LES results with experimental data of a swirl-stabilized combustor, they monitored the volume averaged temperature of the chamber, the OH concentration and the heat release

in the chamber in order to early catch blowout appearance. In the end, they found a good agreement between the results from the two models and the experimental data, but found out that TFLES modeled a less stable flame, which results in a faster blowout event than the one captured with FPV.

In 2013, Zhang *et al.*[11] proposed a new method called Feature-Section-criterion (FSC) for lean blowout prediction of annular combustors. The authors were mostly interested in how lean blowout was influenced by droplet-averaged diameter, flow velocity and temperature. Because of that, they used a simple combustion model, the eddy-dissipation (ED) model, in order to keep low computational costs. Thanks to some experimental data they could validate the FSC method for other engineering applications. A summary of all the cited works is reported in Table 1.1.

Authors (year)	Turbulence model	Combustion model
Wang <i>et al.</i> (2017)[12]	RANS $k - \epsilon$	Laminar Flamelet
Zhang <i>et al.</i> [11]	RANS	Eddy Dissipation (ED)
Akhtar <i>et al.</i> (2018)[7]	RANS $k - \epsilon$, $k - \omega$, RSM, LES	FGM, FPV
Piehl <i>et al.</i> (2018)[8]	LES	Multi-zone model
Esclapez <i>et al.</i> (2015)[9]	LES	FPV
Ma <i>et al.</i> (2019)[10]	LES	FPV and TFLES

Table 1.1: Previous works on LBO investigation

1.2.3 Hybrid methods

During recent years many hybrid method to predict LBO have been developed too. These methods include the use of semi-empirical relations like (1.3) from Lefebvre in addition to numerical simulations with CFD tools. The aim of these

methods is to maintain good accuracy that CFD provides, but without having high computational costs.

An example of hybrid method is the work carried by Soroudi *et al.*[13]. In their work, CFD simulations of reacting flow with simple combustion models have been performed, and the combustor was divided into several perfectly stirred and plug flow reactors and mixers. Then, results have been collected and post-processed to build an Equivalent Reactor Network (ERN) that could predict LBO limits of an industrial gas turbine combustor. After validation on a laboratory scaled combustor, their equivalent reactor method correctly predicted lean blowout of an industrial burner.

Another example is the study conducted by Hu *et al.*[14]. Their work was based on the improved semi-empirical formula from Lefebvre. After conducting several cold flow numerical simulations on many aero engine combustors, they managed to calculate the flame volume, the fraction of dome air and other parameters which were later inserted in Lefebvre's relation and in the end lean blowout was found.

1.2.4 The role of CFD in models validation

According to many studies cited above in section 1.2.2, CFD analysis plays a fundamental role in lean blowout prediction. The main scope of many works was trying to validate CFD codes for LBO prediction. Turbulence models and combustion models were both put to the test, in order to compare their results with experimental data from real combustors.

After analyzing the work done by other researchers in the previous section, some common features have emerged:

- RANS based models are quick and affordable. However, the averaged flow determined by these equations is capable of catching only a global flame extinction. RANS models are often used in hybrid methods, as computational costs are maintained low. Among all the RANS turbulence submodels, realizable $k - \epsilon$ model is the most used one;

- URANS based models are not usually used for this type of analysis;
- LES models are becoming more and more affordable as computational power increases, and many researchers exploit these models. It has been shown that LES based models are able to catch local extinction and are suitable for catching this event which is extremely unsteady;
- When using RANS, the preferred combustion model among researchers is FGM, which is used in this work too;
- When using LES, different combustion models are used, but mostly FPV and TFLES.

1.2.5 Purpose of this work

All the presented works focused on combustors with only one premixed fuel nozzle. Only few works focused on combustors with pilot flame, and there is a lack in literature about model validation of such combustors. Pilot fuel is not premixed, while main fuel is partially premixed and swirled. Validation for these architecture for combustors is not rife at present day. This work is focused on that, trying to make a step for combustors with pilot flame. Numerical simulations will be performed on a reference combustor. The influence of different turbulence models will be tested and investigated: RANS with Realizable $k - \epsilon$,RSM, and URANS. Some user-defined functions will be used, they will tune some flame parameters in order to make flame stretching and quenching closer to reality. In the end, numerical results will be compared to experimental data gathered in the Samara National Research University's Laboratory, where a reference combustor has been tested for different operating conditions.

Chapter 2

Modeling turbulence and combustion

2.1 Turbulence modeling

2.1.1 Definition of turbulence

Fluid regime in nature can be either laminar or turbulent. Laminar flow regimes are completely described by continuity and momentum equations and in some simple cases they can be solved analytically. The kind of flow regime is determined by the *Reynolds number*, an adimensional parameter which represents the balance between inertial effects and viscous effects. It is defined as follows:

$$Re = \frac{\rho V L}{\mu} = \frac{\text{inertial effects}}{\text{viscous effects}} \quad (2.1)$$

where V and L are the reference velocity and length respectively. At low Reynolds number, viscous effects have a great effect influence on the flow and the natural disturbances in the flow is dissipated away, keeping the flow laminar. On high Reynolds number, inertia forces are more relevant and transition to turbulent flow occurs. The motion of the fluid becomes unsteady and chaotic, and the fluid

properties vary randomly in the domain. Turbulent flow is usually associated with the appearance of eddies. Experimentally, these rotational flow structures have been widely captured. Eddies vary in a wide range of scale and velocity. Larger eddies have a characteristic velocity and length which are comparable to the ones of the main flow. So these eddies are dominated by inertial effects. Larger eddies will tend to create smaller eddies until viscous effect will be prevalent. The kinetic energy of the eddies will be dissipated by the viscous forces and converted into thermal energy. This kind of energy conversion related to eddies is called *energy cascade*.

2.1.2 Energy spectrum of turbulence

As said before, turbulent flow has a wide range of length scale and velocity, that's why it is difficult to solve it analytically or numerically. Using the Fourier's analysis, it's possible to convert the domain from time to frequency and from there to extract the turbulent energy spectrum $E(k)$ as a function of the wave number k of the obtained signal. The wave number is the inverse of the length scale and the obtained energy spectrum is shown in Figure 2.1.

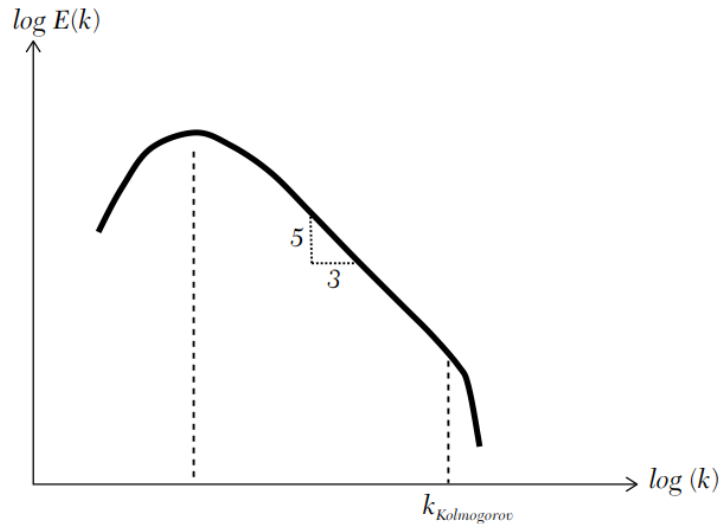


Figure 2.1: Kinetic energy spectrum [15]

Most of the energy of the flow is located at shorter wavelength which corresponds to higher length scales. After the maximum, energy starts to dissipate with a slope of $-\frac{5}{3}$ and it gets steeper as the eddies gets smaller. The exact value of the slope was predicted by Kolmogorov in 1941[16]. According to the turbulence model used, different portions of the energy spectrum are solved. RANS simulations focus on the left part of the graph, near its peak, so they're capable of solving only the large scale eddies. LES simulations can solve the spectrum for shorter scales, near the Kolmogorov's scale, which corresponds to the viscous region. This results in a very high computational cost because smaller eddies are caught in the simulation. However, according to the traditional LES approach a good LES simulation solves around 80% of the turbulent kinetic energy[17]. The remaining 20% is more difficult to compute because eddies are within the cell dimension, so a good sub-grid model (the simple Smagorinsky model and its variants are still probably the most widely used models[17]) can help to catch a slightly higher portion of the energy spectrum of turbulence.

2.1.3 Governing equations

The governing equations of fluid flow are the expressions of the **conservation laws of physics** [18]

- Mass inside a closed fluid system is conserved;
- Newton's second law which tells us that the rate of change of momentum equals the sum of the forces on a fluid particle;
- First law of thermodynamics which tells us that the rate of change of energy is equal to the sum of the rate of heat exchange and the rate of work exchange on a fluid particle.

These principles results in 3 main governing equations, which represents the fundamentals of any fluid analysis. Following, the introduction and discussion of these relations is presented.

Mass conservation

The first step to do in order to write the mass conservation equation is a mass balance on an infinitely little fluid element

$$\text{Rate of change of mass in fluid element} = \text{net rate of mass flux into fluid element}$$

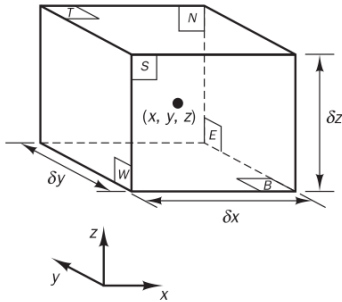


Figure 2.2: Fluid element

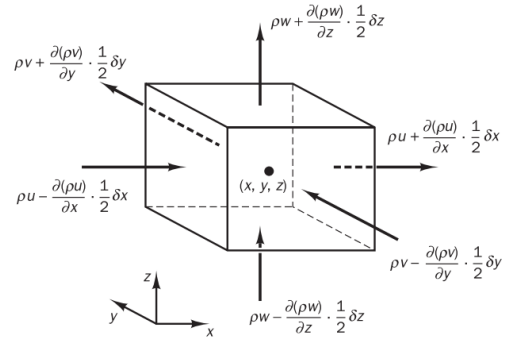


Figure 2.3: Mass fluxes

After writing the mass flux balance across the fluid element according to Figure 2.3, this term is equated to the rate of change of mass in the fluid element. Many terms got simplified and the equation is divided by the volume of the element $\delta x \delta y \delta z$. The final arranged equation is:

$$\frac{\partial \rho}{\partial t} + \frac{(\rho u)}{\partial x} + \frac{(\rho v)}{\partial y} + \frac{(\rho w)}{\partial z} = 0 \quad (2.2)$$

Using the compact vector notation we obtain the differential form of the **continuity equation**:

$$\frac{\partial \rho}{\partial t} + \nabla \cdot (\rho \mathbf{v}) = 0$$

(2.3)

Equation (2.3) is valid for a three-dimensional, unsteady and compressible flow, and expresses conservation of mass. The first term is the time-dependent one while the second is called *convective* term and it's related to net flow of mass across

boundaries of the fluid element.

For an incompressible flow, density ρ is constant and the continuity equation becomes

$$\nabla \cdot \mathbf{v} = 0 \tag{2.4}$$

Momentum equation

The momentum balance equation is based on Newton's second law which states that the rate of change of momentum on a fluid element equals the sum of forces on the particle:

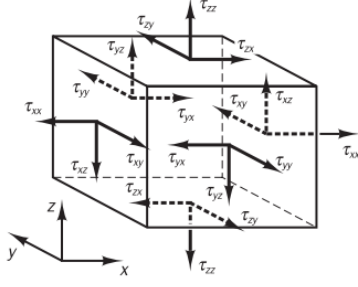
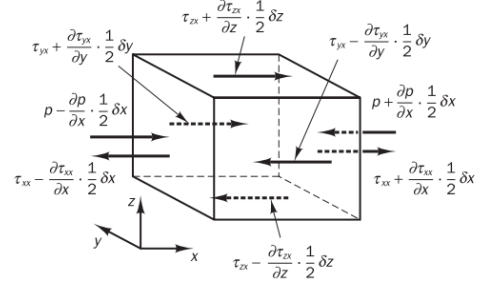
Rate of change of momentum in fluid element = sum of forces on fluid element

The left-hand side of the equation is given by the following expression for the x-axis:

$$\rho \frac{Du}{Dt} \delta x \delta y \delta z \tag{2.5}$$

On the right-hand side of the equation we have to distinguish two types of forces that the fluid particle experiences. They are **body forces** and **surface forces**[19]. The type of body forces that may induce a variation in fluid's momentum are gravity, centrifugal and electromagnetic forces. However, these effects are usually taken into account with an additional source term to the surface forces in the momentum equation. The surface forces that may induce a variation in fluid's momentum are normal stress τ_{ii} (or pressure p) and tangential stress τ_{ij} . The suffices i and j in τ_{ij} indicate that the stress component acts in the j - direction on a surface normal to the i -direction as shown in Figure 2.4.

If a fluid is at rest, there are no tangential stresses and the normal stresses are equal to the negative pressure, which is identical to the thermodynamic pressure. If the fluid is in motion, the equation of state still determines the pressure at every point. It is useful to collect all viscous stresses in a tensor, its components are due only to the motion and vanish at rest [20]. So, the state of stress of a fluid element


Figure 2.4: Stresses on fluid element

Figure 2.5: Stress balance for x-axis

is defined by the tensor $\boldsymbol{\tau}$ which is formed by 9 components:

$$\boldsymbol{\tau} = \begin{bmatrix} \tau_{xx} & \tau_{xy} & \tau_{xz} \\ \tau_{yx} & \tau_{yy} & \tau_{yz} \\ \tau_{zx} & \tau_{zy} & \tau_{zz} \end{bmatrix} \quad (2.6)$$

Due to rotation equilibrium around each side of the fluid element, the tensor is symmetric. In fact:

$$\tau_{yx} = \tau_{xy} \quad ; \quad \tau_{xz} = \tau_{zx} \quad ; \quad \tau_{yz} = \tau_{zy} \quad \rightarrow \quad \tau_{ij} = \tau_{ji}$$

The suffixes i and j denotes that the viscous stress is acting on the face normal to direction i and along direction j . Forces which are aligned with the j -direction gets a positive sign, otherwise forces along the opposite direction get a negative sign.

Balance equations for forces on each axis of the fluid element in Figure 2.5 are written. After dividing by the volume of the fluid element $\delta x \delta y \delta z$, a final form of momentum balance equation for each axis is obtained. These are gathered into a single vectorial form known as the Lagrangian form of the **momentum equation**:

$$\rho \frac{D\mathbf{v}}{Dt} = -\nabla p + \nabla \cdot \boldsymbol{\tau} + \sum \mathbf{F}^{body\ forces} \quad (2.7)$$

Relation between viscous stress and deformation

In many fluid flow, a model for viscous stresses is introduced, which can be expressed as a function of local deformation rate or strain rate. According to **Newton's law of viscosity**, the normal and tangential stress components are given by:

$$\begin{aligned}\tau_{xx} &= \lambda \nabla \cdot \mathbf{v} + 2\mu \frac{\partial u}{\partial x} \\ \tau_{yy} &= \lambda \nabla \cdot \mathbf{v} + 2\mu \frac{\partial v}{\partial y} \\ \tau_{zz} &= \lambda \nabla \cdot \mathbf{v} + 2\mu \frac{\partial w}{\partial z} \\ \tau_{xy} = \tau_{yx} &= \mu \left(\frac{\partial v}{\partial x} + \frac{\partial u}{\partial y} \right) \\ \tau_{yz} = \tau_{zy} &= \mu \left(\frac{\partial w}{\partial y} + \frac{\partial v}{\partial z} \right) \\ \tau_{zx} = \tau_{xz} &= \mu \left(\frac{\partial u}{\partial z} + \frac{\partial w}{\partial x} \right)\end{aligned}$$

Or, in a more compact way:

$$\tau_{ij} = \mu \left(\frac{\partial u_i}{\partial x_j} + \frac{\partial u_j}{\partial x_i} \right) + \delta_{ij} \lambda \nabla \cdot \mathbf{v} \quad (2.8)$$

where δ_{ij} is Kronecker's delta ($\delta_{ij} = 1$ if $i = j$ and $\delta_{ij} = 0$ otherwise). Moreover, equation (2.8) involves two constants of proportionality: the first (dynamic) viscosity μ , to relate stresses to linear deformations, and the second viscosity λ to relate stresses to the volumetric deformation. λ is called *Bulk Viscosity* and not much is known about it, since its effect is small. Fluids that obey to this relation are called **Newtonian fluids**. These are fluids where viscous stresses are proportional to the rate of deformation.

Stokes' hypothesis

Following a suggestion by Stokes, it is customary to assume that the two coefficients of viscosity appearing in (2.8) are linked by the relation

$$\lambda + \frac{2}{3}\mu = 0 \quad \rightarrow \quad \lambda = -\frac{2}{3}\mu \quad (2.9)$$

This is known as Stokes' hypothesis [21] and it has been widely used for analysis of compressible fluids. This hypothesis makes the fluid analysis rather simple, but its truthfulness and validity were widely discussed in literature.

Energy equation

The energy equation is governed by the first law of thermodynamics which states that energy can be neither created nor destroyed during a process; it can only change from one form (mechanical, kinetic, chemical, etc.) into another. Consequently, the sum of all forms of energy in an isolated system remains constant [22]. In other words, this fundamental law states that the rate of change of internal energy is equal to the net rate of work exchanged with the fluid particle plus the net rate of heat exchanged.

$$\text{Rate of change of energy} = \text{net rate of work exchanged} + \text{net rate of heat exchanged}$$

E is the total energy per unit volume given by:

$$E = \left(e + \frac{v^2}{2} + \text{potential energy} + \dots \right)$$

and e is the internal energy per unit mass. The first contribution to the particle's energy is the **rate of work exchanged** by the particle. As for the momentum equation, there is a distinction between *surface forces* and *body forces*. The contribution of body forces is taken into account with a source term as for momentum

equation while the one of surface forces is given by the product of force and velocity component according to the direction of the force. A balance equation is written in each direction, one for each axis. The net rate of energy exchanged is given by the sum of these equations.

Regarding the heat exchanged, we consider a heat flux vector \mathbf{q} with 3 components.

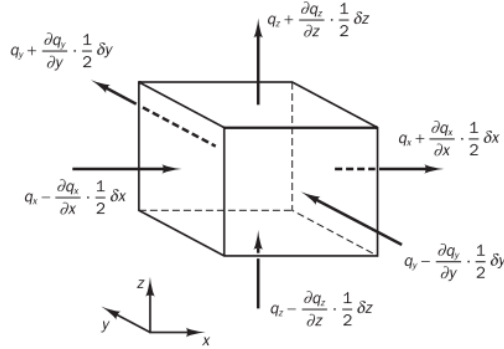


Figure 2.6: Heat flux in a fluid element

Heat exchange contributes to the exchange of energy, so a heat balance equation is written for each axis, too. The total rate of heat exchanged is the sum of the latter.

Gathering all these contributions together, it's possible to write the final form of the **energy equation**:

$$\boxed{\rho \frac{DE}{Dt} = -\nabla \cdot (p\mathbf{v}) + \nabla \cdot (\boldsymbol{\tau} \cdot \mathbf{v}) - \nabla \cdot \mathbf{q} + S_E} \quad (2.10)$$

For compressible flows it is usually found a version of the conservation of energy where dependence from *enthalpy* is explicit. The specific enthalpy h and the total enthalpy h^0 are defined as:

$$h = i + \frac{p}{\rho} \quad ; \quad h^0 = h + \frac{1}{2}(u^2 + v^2 + w^2)$$

where i is the internal energy of the fluid. Combining the latter, it's possible to

explicit the dependence of the specific energy on enthalpy as follows:

$$h^0 = i + \frac{p}{\rho} + \frac{1}{2}(u^2 + v^2 + w^2) = E + \frac{p}{\rho} \quad (2.11)$$

Rearranging equation (2.10) according to the definition of total enthalpy in (2.11), a form of the equation for the total enthalpy is found:

$$\rho \frac{Dh^0}{Dt} = \frac{\partial p}{\partial t} + \nabla \cdot (\boldsymbol{\tau} \cdot \mathbf{v}) - \nabla \cdot \mathbf{q} + S_{h^0} \quad (2.12)$$

Conservation Law for single species

The continuity equation expresses the overall mass conservation of the flow and no distinction is made between different chemical species in the flow. However, if the flow is expected to be a reacting flow, as it is in this work, in addition to mass conservation equation, the conservation law for chemically reacting flow is necessary[23].

Using the integral formulation:

$$\left(\frac{dm_k}{dt} \right)_{system} = - \int_S \mathbf{j}_k \cdot \mathbf{n} dA + \int_V \omega_k W_k dV \quad (2.13)$$

where \mathbf{j}_k is the diffusive mass flux of chemical species k, ω_k is the production rate of chemical species k and W_k is its molecular weight Thanks to the Reynolds transport theorem and to the Gauss divergence one, relation (2.13) becomes the **species-continuity equation**[23]:

$$\boxed{\rho \frac{DY_k}{Dt} = -\nabla \cdot \mathbf{j}_k + \omega_k W_k} \quad (2.14)$$

where Y_k is the mass fraction of the k-th species.

2.1.4 Navier-Stokes equations

For a Newtonian fluid, characterized by the viscous stresses in eq.(2.8), the momentum balance equation (2.7) together with the continuity equation (2.3) constitutes the set of governing equations for a fluid, called the **Navier-Stokes equations**, named after the two nineteenth-century scientists who derived them independently:

$$\text{mass:} \quad \frac{\partial \rho}{\partial t} + \nabla \cdot (\rho \mathbf{v}) = 0 \quad (2.15)$$

$$\text{x-momentum:} \quad \rho \frac{Du}{Dt} = -\frac{\partial p}{\partial x} + \frac{\partial \tau_{xx}}{\partial x} + \frac{\partial \tau_{yx}}{\partial y} + \frac{\partial \tau_{zx}}{\partial z} + S_{M_x} \quad (2.16)$$

$$\text{y-momentum:} \quad \rho \frac{Dv}{Dt} = -\frac{\partial p}{\partial y} + \frac{\partial \tau_{xy}}{\partial x} + \frac{\partial \tau_{yy}}{\partial y} + \frac{\partial \tau_{zy}}{\partial z} + S_{M_y} \quad (2.17)$$

$$\text{z-momentum:} \quad \rho \frac{Dw}{Dt} = -\frac{\partial p}{\partial z} + \frac{\partial \tau_{xz}}{\partial x} + \frac{\partial \tau_{yz}}{\partial y} + \frac{\partial \tau_{zz}}{\partial z} + S_{M_z} \quad (2.18)$$

These are non-linear partial differential equations which cannot (yet) be solved analytically. Finding a solution with numerical methods is the common way of solving the set of these equations. The introduction of approximations and simplifications to the studied case can significantly reduce computational cost. The set of Navier-Stokes equations and the Energy equation (2.10) needs to be closed and it contains 7 unknown variables: \mathbf{v}, ρ, p, E , viscous stresses $\boldsymbol{\tau}$ and the heat flux q . Thus it's necessary to introduce some constitutive equations. The gas state equation together with the Fourier's law for the heat flux are used to accomplish this goal.

2.2 Reynolds averaged Navier-Stokes equations (RANS)

Turbulence is associated with the existence of random fluctuations in the fluid. The flow can be decomposed in a mean signal and a fluctuating one. This approach

presents an attractive way to characterize a turbulent flow by the mean values of flow properties (u, v, w, p , etc.) with its corresponding statistical fluctuating property (u_0, v_0, w_0, p_0 , etc.)[24] Recalling the Navier-Stokes equations for a viscous incompressible fluid with constant properties, using the Einstein notation, these are:

$$\frac{\partial u_i}{\partial x_i} = 0 \quad (2.19)$$

$$\frac{\partial u_i}{\partial t} + u_j \frac{\partial u_i}{\partial x_j} = -\frac{1}{\rho} \frac{\partial p}{\partial x_i} + \nu \frac{\partial^2 u_i}{\partial x_j \partial x_j} \quad (2.20)$$

where u_i are the scalar components of the instantaneous velocity vector \mathbf{v} , ν is the kinematic viscosity and p is the pressure divided by the density of the fluid. Here body forces have been neglected. The time-dependent term on the left-hand side is retained for convenience, though it is zero for a stationary flow.

In 1895 Osborne Reynolds proposed a way to decompose a variable into a mean part and a fluctuating one. This mathematical technique is called *Reynolds decomposition* and nowadays it represents the first step in order to model turbulent flows. In particular, every variable (like velocity u_i and pressure p) can be written as the sum of a time-averaged value and a fluctuating one as following[25]:

$$\phi(x_i, t) = \Phi(x_i) + \phi'(x_i, t) \quad (2.21)$$

where

$$\Phi(x_i) = \lim_{T \rightarrow \infty} \int_0^T \phi(x_i, t) dt \quad (2.22)$$

The averaging interval T must be larger to the usual time scales of fluctuations. This kind of averaging process is called *Reynolds averaging*. This decomposition is applied to velocity u_i and pressure p as follows:

$$u_i = U_i + u'_i \quad ; \quad p = P + p'$$

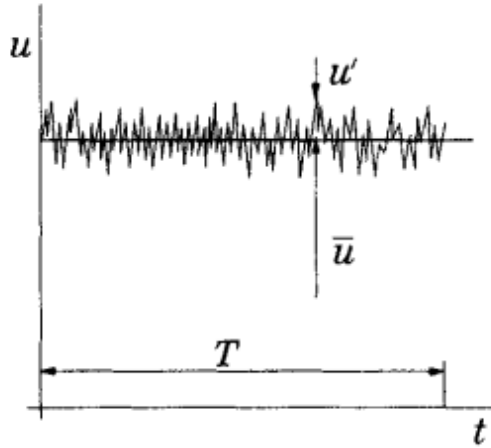


Figure 2.7: Time averaging of a steady flow[25]

Substituting the decomposed velocity and pressure in the Navier-Stokes equations and averaging we obtain the so called **Reynolds Averaged Navier-Stokes equations (RANS)**:

$$\frac{\partial U_i}{\partial x_i} = 0 \quad (2.23)$$

$$\frac{\partial U_i}{\partial t} + U_j \frac{\partial U_i}{\partial x_j} = -\frac{1}{\rho} \frac{\partial P}{\partial x_i} + \nu \frac{\partial^2 U_i}{\partial x_j \partial x_j} - \frac{\partial \overline{u'_i u'_j}}{\partial x_j} \quad (2.24)$$

Averaging the convective term, the fluctuating velocity gives rise to the extra term containing the correlation between the components of the fluctuating velocities. This extra term is a tensor, called *Reynolds Stress Tensor*, and it acts like an additional fictitious stress tensor.

$$R_{ij} = -\rho \overline{u'_i u'_j} = -\rho \begin{bmatrix} \overline{u_1'^2} & \overline{u_1' u_2'} & \overline{u_1' u_3'} \\ \overline{u_1' u_2'} & \overline{u_2'^2} & \overline{u_2' u_3'} \\ \overline{u_1' u_3'} & \overline{u_2' u_3'} & \overline{u_3'^2} \end{bmatrix}$$

Some features of the Reynolds tensor are:

- it is *symmetric*, so $R_{ij} = R_{ji}$;
- the diagonal components are averaged co-correlation of velocity fluctuations which act like *normal stresses*;
- the off-diagonal components are cross-correlation of velocity fluctuations which act like *shear stresses*.

The presence of the Reynolds stresses in the RANS system of equations means that some approximations are required to assure the closure of the system.

Boussinesq hypothesis

In order to close the system and to find known expression for the Reynolds stress tensor, Boussinesq in 1877 [26] proposed to relate the Reynolds stress to the mean velocity gradients. These are related through the *turbulent viscosity* or *eddy viscosity* μ_t :

$$R_{ij} = \mu_t(\bar{u}_{i,j} + \bar{u}_{j,i}) - \frac{2}{3}\rho k\delta_{ij} \quad (2.25)$$

where δ_{ij} is Kronecker's delta and $k = \frac{\overline{u'_i u'_i}}{2} = \frac{1}{2}(\overline{u'_x u'_x} + \overline{u'_y u'_y} + \overline{u'_z u'_z})$ is the *turbulent kinetic energy* per unit mass. Relation (2.25) represents a first approximation of the Reynolds stress tensor and it is still used nowadays in many turbulence models as showed below.

2.2.1 Mixing length model

Although it is not used in this work, it is worth citing this first turbulence model as it represents the origins of turbulence modeling.

The *mixing-length model* was the first model proposed to approximate the eddy viscosity. In 1925 Prandtl[27] proposed this theory by analogy with the kinetic

theory of gases so that the turbulent viscosity μ_t can be expressed as:

$$\mu_t = \rho l_m^2 \left| \frac{\partial U}{\partial y} \right| \quad (2.26)$$

By substituting the expression of μ_t in (2.25), the turbulent Reynolds stress is described by:

$$-\overline{\rho u'_i u'_j} = \rho l_m^2 \left| \frac{\partial U}{\partial y} \right| \frac{\partial U}{\partial y} \quad (2.27)$$

The mixing-length model is applicable to all turbulent flows, but there is a major drawback: the value of the mixing length l_m has to be specified according to the geometry of the flow. If the flow is much complex and not well studied yet, the specification of l_m brings large guesswork and consequently, little accuracy from the results is expected.

2.2.2 Standard $k - \epsilon$ model

Although this model is not directly employed in this work, it is worth introducing it as it represents the basis for the one used to model turbulence. The standard $k - \epsilon$ model was developed in the 1970s by Jones and Lauder[28] and is one of the most used, analyzed, and validated turbulence models. Its main innovation is to solve 2 additional transport equations, one for the turbulent kinetic energy k and one for its rate of dissipation ϵ . Literature about the derivation of these transport equations is very wide and can be found on Wilcox's book[29]. The standard $k - \epsilon$ model uses the following transport equations for k and ϵ :

$$\frac{\partial(\rho k)}{\partial t} + U_j \frac{\partial(\rho k)}{\partial x_j} = \frac{\partial}{\partial x_j} \left[\left(\mu + \frac{\mu_t}{\sigma_k} \right) \frac{\partial k}{\partial x_j} \right] - \overline{\rho u'_i u'_j} \frac{\partial U_i}{\partial x_j} - \rho \epsilon \quad (2.28)$$

$$\frac{\partial(\rho \epsilon)}{\partial t} + U_j \frac{\partial(\rho \epsilon)}{\partial x_j} = \frac{\partial}{\partial x_j} \left[\left(\mu + \frac{\mu_t}{\sigma_\epsilon} \right) \frac{\partial \epsilon}{\partial x_j} \right] - C_{1\epsilon} \frac{\epsilon}{k} \overline{\rho u'_i u'_j} \frac{\partial U_i}{\partial x_j} - C_{2\epsilon} \rho \frac{\epsilon^2}{k} \quad (2.29)$$

In addition to (2.28) and (2.29), the turbulent viscosity μ_t is calculated as following:

$$\mu_t = C_\mu \rho \frac{k^2}{\epsilon} \quad (2.30)$$

where $\sigma_k, \sigma_\epsilon, C_{1\epsilon}, C_{2\epsilon}, C_\mu$ are constants called *model constants*. Looking at equation (2.28), each of its term has a different meaning:

- $\frac{\partial(\rho k)}{\partial t}$ is the time-dependent term;
- $U_j \frac{\partial k}{\partial x_j}$ is the transport of k by convection inside the flow;
- $\frac{\partial}{\partial x_j} \left[\left(\mu + \frac{\mu_t}{\sigma_k} \right) \frac{\partial k}{\partial x_j} \right]$ is the transport of k by diffusion inside the flow;
- $\overline{\rho u'_i u'_j \frac{\partial U_i}{\partial x_j}}$ represents the production of turbulent kinetic energy k ;
- $\rho \epsilon$ is the term that acts as dissipation of k . It gives a measure of the rate at which turbulent kinetic energy is dissipated.

Model constants

The value of model constants $\sigma_k, \sigma_\epsilon, C_{1\epsilon}, C_{2\epsilon}, C_\mu$ has varied as years go by since their first value proposed by Jones and Launder in 1972[28]. Nowadays, CFD softwares uses default values of these constants, according to Launder and Sharma(1974)[30].

σ_k	σ_ϵ	$C_{1\epsilon}$	$C_{2\epsilon}$	C_μ
1.0	1.3	1.44	1.92	0.09

Table 2.1: Model constants - Standard $k - \epsilon$ [30]

These default values have been determined from experiments for fundamental turbulent flows. They have been found to work fairly well for a wide range of flows.

2.2.3 Realizable $k - \epsilon$ model

A new $k - \epsilon$ model, called *Realizable $k - \epsilon$ model*, was proposed in 1994 by Shih *et al.*[31] and will be used in many simulations in this work as it is the most appropriate for the studied case. The standard $k - \epsilon$ model was shown to have some limitations for flows with a high mean shear rate or with separation, while performing well for boundary layer flows. The main problem for the standard $k - \epsilon$ model was that in certain conditions, the normal stresses can become negative and this results in a violation of the Schwarz' inequality. It's possible to show how this is possible by taking into account the Boussinesq hypothesis (2.25) and the eddy viscosity definition (2.30) and looking at the normal component. The following expression is obtained:

$$\overline{u'^2} = \frac{2}{3}k - 2C_\mu \frac{k^2}{\epsilon} \frac{\partial U}{\partial x} \quad (2.31)$$

The normal stress $\overline{u'^2}$, which is positive by definition, can become a negative quantity (and so "non-realizable") when the strain rate is large enough to satisfy:

$$\frac{k}{\epsilon} \frac{\partial U}{\partial x} > \frac{1}{3C_\mu} \approx 3.7 \quad (2.32)$$

assuming $C_\mu = \text{const} = 0.09$ as done in the standard $k - \epsilon$ model. In short, the main differences between this model and the standard $k - \epsilon$ turbulence model are:

- a new formulation for turbulent viscosity μ_t ;
- a modified transport equation for the eddy dissipation rate ϵ

Turbulent viscosity μ_t

The new formulation of eddy viscosity starts from a new formulation of C_μ . In particular, the definition of eddy viscosity, like in the standard model, still holds:

$$\mu_t = C_\mu \rho \frac{k^2}{\epsilon} \quad (2.33)$$

But this time, C_μ is no more constant. Reynolds[32] and Shih *et al.* [33] proposed a new formulation for C_μ as follows:

$$C_\mu = \frac{1}{A_0 + A_s U^{(*)} \frac{k}{\epsilon}} \quad (2.34)$$

where

$$\begin{aligned} U^{(*)} &= \sqrt{S_{ij}S_{ij} + \tilde{\Omega}_{ij}\tilde{\Omega}_{ij}} \\ \tilde{\Omega}_{ij} &= \Omega_{ij} - 2\epsilon_{ijk}\omega_k \\ \Omega_{ij} &= \bar{\Omega}_{ij} - \epsilon_{ijk}\omega_k \end{aligned} \quad (2.35)$$

and

- $S_{ij} = \frac{1}{2} \left(\frac{\partial U_i}{\partial x_j} + \frac{\partial U_j}{\partial x_i} \right)$ is a symmetric tensor called the *strain-rate tensor*;
- $\Omega_{ij} = \frac{1}{2} \left(\frac{\partial U_i}{\partial x_j} - \frac{\partial U_j}{\partial x_i} \right)$ is a anti-symmetric tensor called the *vorticity tensor*;
- $\bar{\Omega}_{ij}$ is the mean rate of rotation tensor viewed in a moving reference frame with angular velocity ω_k [31];
- $A_0 = 4.04$ is a constant;
- A_s is determined by:

$$\begin{aligned} A_s &= \sqrt{6} \cos \phi \quad ; \quad \phi = \frac{1}{3} \arccos(\sqrt{6}W) \\ W &= \frac{S_{ij}S_{jk}S_{ki}}{\tilde{S}^3} \quad ; \quad \tilde{S} = \sqrt{S_{ij}S_{ij}} \end{aligned}$$

Using all the previous relations, it can be seen that C_μ is no more constant and depends on k , the mean strain and rotation rates, ϵ and the angular velocity of the system. From equation (2.34), the value used in the standard $k - \epsilon$ model ($C_\mu = 0.09$) is obtained in the inertial sublayer of an equilibrium boundary layer.

Transport equation for ϵ

Another main difference between the standard $k - \epsilon$ model and the Realizable one, is a different formulation of the transport equation for ϵ .

$$\begin{aligned} \frac{\partial(\rho\epsilon)}{\partial t} + U_j \frac{\partial(\rho\epsilon)}{\partial x_j} = \frac{\partial}{\partial x_j} \left[\left(\mu + \frac{\mu_t}{\sigma_\epsilon} \right) \frac{\partial \epsilon}{\partial x_j} \right] + \\ + \rho C_1 S \epsilon - \rho C_2 \frac{\epsilon^2}{k + \sqrt{\frac{\mu_t}{\rho}} \epsilon} + C_{1\epsilon} \frac{\epsilon}{k} C_{3\epsilon} G_b \end{aligned} \quad (2.36)$$

where G_b is the generation of k due to buoyancy effects. Moreover:

$$C_1 = \max \left[0.43, \frac{\eta}{\eta + 5} \right] \quad ; \quad \eta = S \frac{k}{\epsilon} \quad ; \quad S = \sqrt{2S_{ij}S_{ij}}$$

The main difference between the standard transport equation for ϵ (2.29) and the new one (2.36) is the *source term*. This term is the second on the right-hand side of equation (2.36), and doesn't contain the Reynolds stresses in the new new formulation. Shih *et al.*[31] believed that this formulation describes the turbulent vortex stretching and dissipation terms more appropriately compared to the standard $k - \epsilon$ model.

Model constants

As for the standard $k - \epsilon$ model, this model implements some model constants. The only main difference from the standard model is that C_μ is no more a constant but it's determined by equation(2.34). The value of the model constants is the following:

σ_k	σ_ϵ	$C_{1\epsilon}$	$C_{2\epsilon}$
1.0	1.2	1.44	1.9

Table 2.2: Model constants - Realizable $k - \epsilon$ model [31]

2.2.4 Reynolds stress model (RSM)

The Reynolds stress model (RSM) was initially developed by Launder *et al.* in 1975[34] and is used in this work during certain simulations. Nowadays, this turbulence model represents the most complex RANS turbulence model available. The RSM has greater potential in computing accurately the effects of streamline curvature, rotation, swirl and quick changes in strain rate of the fluid. The most challenging contribute to model are the pressure-strain and dissipation-rate terms, and because of that, this model still lacks in accuracy in certain predictions. The main feature of the Reynolds stress model is that it closes the RANS equations without the Boussinesq hypothesis, but instead solving transport equations for the Reynolds stresses, plus another one for the dissipation rate.

Transport equations for Reynolds stresses

Following the work from Launder *et al.*[35], the transport equations for Reynolds stresses cited above can be written as:

$$\begin{aligned}
 \frac{\partial}{\partial t}(\rho \overline{u'_i u'_j}) + \frac{\partial}{\partial x_k}(\rho u_k \overline{u'_i u'_j}) = & - \frac{\partial}{\partial x_k} \left[\overline{\rho u'_i u'_j u'_k} + \overline{p'(\delta_{jk} u'_i + \delta_{ik} u'_j)} \right] + \quad (2.37) \\
 & + \frac{\partial}{\partial x_k} \left[\mu \frac{\partial}{\partial x_k} (\overline{u'_i u'_j}) \right] + \\
 & - \rho \left(\overline{u'_i u'_k} \frac{\partial u_j}{\partial x_k} + \overline{u'_j u'_k} \frac{\partial u_i}{\partial x_k} \right) + \\
 & - \rho \beta \left(g_i \overline{u'_j \theta} + g_j \overline{u'_i \theta} \right) + \\
 & + p' \left(\frac{\partial u'_i}{\partial x_j} + \frac{\partial u'_j}{\partial x_i} \right) + \\
 & - 2\mu \frac{\partial u'_i}{\partial x_k} \frac{\partial u'_j}{\partial x_i}
 \end{aligned}$$

where:

- $\frac{\partial}{\partial x_k}(\rho u_k \overline{u'_i u'_j})$ is the transport of the Reynolds stresses by convection processes;
- $D_{T,ij} = -\frac{\partial}{\partial x_k} \left[\overline{\rho u'_i u'_j u'_k} + \overline{p'(\delta_{jk} u'_i + \delta_{ik} u'_j)} \right]$ is the transport by diffusion processes;
- $D_{L,ij} = +\frac{\partial}{\partial x_k} \left[\mu \frac{\partial}{\partial x_k} (\overline{u'_i u'_j}) \right]$ is the molecular diffusion;
- $P_{ij} = -\rho \left(\overline{u'_i u'_k} \frac{\partial u_j}{\partial x_k} + \overline{u'_j u'_k} \frac{\partial u_i}{\partial x_k} \right)$ is the production term of Reynolds stresses;
- $G_{ij} = -\rho \beta \left(g_i \overline{u'_j \theta} + g_j \overline{u'_i \theta} \right)$ is the production term by buoyancy effects;
- $\varphi_{ij} = p' \left(\frac{\partial u'_i}{\partial x_j} + \frac{\partial u'_j}{\partial x_i} \right)$ is the pressure-strain term, which is object of much modeling work;
- $\epsilon_{ij} = -2\mu \frac{\partial u'_i}{\partial x_k} \frac{\partial u'_j}{\partial x_i}$ is the dissipation term.

However, among all this terms, only few of them require modeling. These are $D_{T,ij}$, G_{ij} , φ_{ij} and ϵ_{ij} .

Turbulent diffusion $D_{T,ij}$ is conventionally modeled using Daly and Harlow's relation[36]:

$$D_{T,ij} = C_S \frac{\partial}{\partial x_k} \left(\rho \frac{\overline{k u'_k u'_l} \frac{\partial \overline{u'_i u'_j}}{\partial x_l}}{\epsilon} \right) \quad (2.38)$$

but this relation has been showed to generate some numerical instabilities especially in 3D simulations. Lien *et al.* proposed and used a simplified version of equation (2.38), which is not so sensible to numerical instabilities as before[37]:

$$D_{T,ij} = \frac{\partial}{\partial x_k} \left(\frac{\mu_t}{\sigma_k} \frac{\partial \overline{u'_i u'_j}}{\partial x_k} \right) \quad (2.39)$$

where according to the work of Lien *et al.*, σ_k is equal to 0.82, which is way different from the value 1 used in the standard and realizable $k - \epsilon$ model.

The buoyancy production term has to be modeled, too. Exploiting the definition of thermal expansion β , it's possible to get the following expression:

$$G_{ij} = -\frac{\mu_t}{\rho P r_t} \left(g_i \frac{\partial \rho}{\partial x_j} + g_j \frac{\partial \rho}{\partial x_i} \right) \quad (2.40)$$

where g_i is the component of the gravitational vector in the i -th direction and Pr_t is the Prandtl number. A detailed description of the obtained relation is available in Launder's work[38].

The pressure-strain term of equation (2.37), denoted by φ_{ij} is the most difficult part to model in the Reynolds stress model and it has been the main topic of discussion in many papers and articles. Although this term can be expressed in a linear or in a quadratic model, the most spread version, used in many commercial CFD softwares like Fluent, is a slightly improved version of the original one proposed by Gibson and Launder in 1978[38]. This approach exploits a decomposition in three terms:

$$\varphi_{ij} = \varphi_{ij,1} + \varphi_{ij,2} + \varphi_{ij,w} \quad (2.41)$$

where the first term $\varphi_{ij,1}$ is usually referred as the slow pressure-strain term, while the second term $\varphi_{ij,2}$ is the rapid pressure-strain term. In the end, the last term $\varphi_{ij,w}$ is the wall-reflection term. The slow-pressure term can be modeled as:

$$\varphi_{ij,1} = -C_1 \rho \frac{\epsilon}{k} \left(\overline{u'_i u'_j} - \frac{2}{3} \delta_{ij} k \right) \quad (2.42)$$

with $C_1 = 1.8$, while the rapid pressure-strain term $\varphi_{ij,2}$ can be modeled as:

$$\varphi_{ij,2} = -C_2 \left[\left(P_{ij} + F_{ij} + \frac{5}{6} G_{ij} - C_{ij} \right) - \frac{2}{3} \delta_{ij} \left(P + \frac{5}{6} G - C \right) \right] \quad (2.43)$$

with $C_2 = 0.6$, while P_{ij}, F_{ij}, G_{ij} and C_{ij} are the variables from the Reynolds stresses transport equation (2.37), $P = \frac{1}{2} P_{kk}$, $G = \frac{1}{2} G_{kk}$ and $C = \frac{1}{2} C_{kk}$.

In the end, the last term of equation (2.41), the wall-reflection term $\varphi_{ij,w}$, can be modeled as:

$$\begin{aligned} \varphi_{ij,w} = & C'_1 \frac{\epsilon}{k} \left(\overline{u'_k u'_m n_k n_m} \delta_{ij} - \frac{3}{2} \overline{u'_i u'_k n_j n_k} - \frac{3}{2} \overline{u'_j u'_k n_i n_k} \right) \frac{C_l k^{3/2}}{\epsilon d} + \\ & + C'_2 \left(\varphi_{km_2} n_k n_m \delta_{ij} - \frac{3}{2} \varphi_{ik,2} n_j n_k - \frac{3}{2} \varphi_{jk,2} n_i n_k \right) \frac{C_l k^{3/2}}{\epsilon d} \end{aligned} \quad (2.44)$$

σ_ϵ	$C_{1\epsilon}$	$C_{2\epsilon}$	$C_{3\epsilon}$
1.0	1.44	1.92	eq(2.46)

Table 2.3: Model constants - RSM[39]

with $C'_1 = 0.5$, $C'_2 = 0.3$, d is the normal distance from the wall, $C_l = C_\mu^{3/4}/\kappa$ with $\kappa = 0.4187$ is the Von Kharman constant and n_k is the x_k component of the unit normal to the wall.

Transport equation for ϵ

Beside the set of transport equations for the Reynolds stresses, the RSM requires the resolution of a transport equation for ϵ as well. However, this transport equation is very similar to the one used in the standard $k - \epsilon$ model[39]:

$$\frac{\partial(\rho\epsilon)}{\partial t} + \frac{\partial(\rho\epsilon u_i)}{\partial x_i} = \frac{\partial}{\partial x_j} \left[\left(\mu + \frac{\mu_t}{\sigma_\epsilon} \right) \frac{\partial \epsilon}{\partial x_j} \right] - C_{1\epsilon} \frac{1}{2} [P_{ii} + C_{3\epsilon} G_{ii}] \frac{\epsilon}{k} - C_{2\epsilon} \rho \frac{\epsilon^2}{k} \quad (2.45)$$

where P_{ii} and G_{ii} are the variables from the Reynolds stresses transport equation (2.37), while $C_{1\epsilon}$, $C_{2\epsilon}$ and $C_{3\epsilon}$ are model constants.

Model constants

Also this model uses model constants, which have varied over the years. However, $C_{3\epsilon}$ is not actually constant, but in this model is evaluated according to the following relation[40]:

$$C_{3\epsilon} = \tanh \left| \frac{v}{u} \right| \quad (2.46)$$

where v and u are components of velocity, parallel and perpendicular to the gravitational field.

The other model constants are expressed in the following table:

2.2.5 URANS formulation

URANS equations are also used in this work to simulate lean blowout. In order to better capture the dynamics of such complex phenomenon, it is appropriate to use this unsteady method.

URANS formulation stands for Unsteady-RANS and exploits Reynolds averaging in a similar way to RANS equation as showed in section 2.2. However, as explained by Ferziger et al.[25] if the flow is unsteady, ensemble averaging must be used instead of time averaging. The Reynolds decomposition stands:

$$\phi(x_i, t) = \Phi(x_i, t) + \phi'(x_i, t) \quad (2.47)$$

but with ensemble averaging Φ depends both on time and space, as the following averaging process holds:

$$\Phi(x_i, t) = \lim_{N \rightarrow \infty} \sum_{N=1}^N \phi(x_i, t) dt \quad (2.48)$$

where N is the number of members of ensembles and must be large enough to eliminate the effect of fluctuations. The results of ensemble averaging is shown in Figure 2.8. It is clear how the mean flow is not steady, so time averaging as employed in RANS is not appropriate for these types of flows.

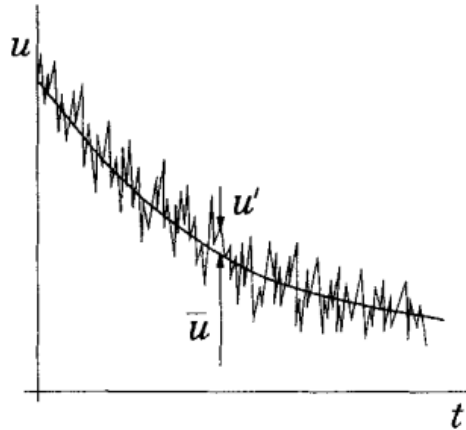


Figure 2.8: Ensemble averaging of an unsteady flow[25]

2.3 Combustion modeling

Combustion modeling is an important part of combustion related phenomena as this work. Solving the set of differential equations for conservation of mass, momentum, energy and chemical species is the way to simulate combustion processes. Usually, the number of species is high as well as the number of reactions, and this leads to a strong coupling between the equations. Thus, the set of equations is stiff and numerical strategies have to be implemented to reach the goal. In the last decades, many methods have been developed, with the common aim of reducing computational costs. The fastest and easiest way of keeping computational costs low is by simplifying the chemical reaction model by using a global reaction mechanism, which takes into account only few equations to solve and where fuel and oxidizer are simply turned into products. However, this kind of models are suitable only for global studies, as they suffer from a big lack of accuracy. More recent methods, takes into account few global reaction steps, but they suffer from the same problems. Other methods exploit the assumption that in a global reaction, there are many processes whose time scales are much smaller than the flow scale, thus they can be decoupled and computational efficiency can be increased. The most outstanding method of this kind is the computational singular perturbation (CSP)[41] and the

intrinsic low dimensional manifold(ILDM)[42].

As said in section 1.2.5, this work involves partially premixed combustion. Thus a combustion model which is specifically developed for this type of combustion regime is used and presented in section 2.3.2.

2.3.1 Combustion regimes

There are two main kind of combustion regimes: premixed and non-premixed, depending on whether fuel and air are mixed before combustion, or mixed by diffusion in the flame zone. An example of both regimes is the Bunsen burner shown in Figure 2.9. Air can be mixed or not prior to combustion, generating non-premixed or premixed regime. The amount of air to be mixed can be set with a valve at the base of the burner. If the air valve is closed, transport phenomena as diffusion and convection make the gas to mix with the surrounding air and the flame can develop once that enough mixing is ensured. This non-premixed flame is usually colder than premixed ones and produce more soot as indicated by the large yellow portion of the flame. As more air is premixed to the gas, the flame becomes hotter and more blue, as shown by Figure 2.9.

In the past, combustors have been operated in the non-premixed regime. This regime ensures safety and stability of the combustion process. Moreover, it provides very good energy conversion efficiency since it is possible to have a good control on CO emissions alongside with high combustion efficiencies and low-pressure losses[7]. Conversely, premixed combustion regime ensures low pollutant emission like NOx but allows to be concerned about critical phenomena like lean blowout. As said before, the combustion regime of this work actually belongs to a third type of regime, collocated in between the non-premixed and the premixed one: the **partially premixed** combustion regime. This regime involves premixed flames with non-uniform fuel-oxidizer mixtures and it incorporates features of both premixed and non-premixed regimes.

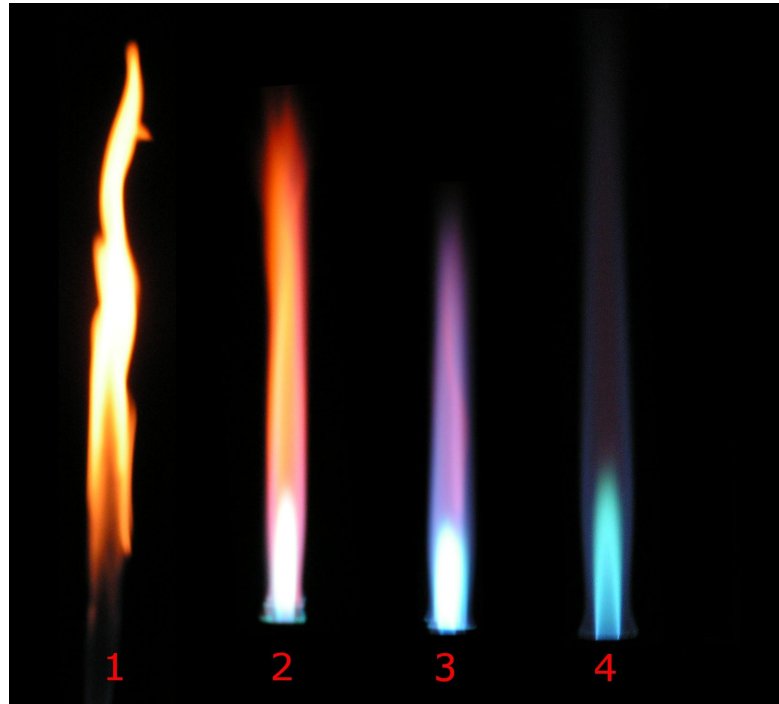


Figure 2.9: Different flame types of Bunsen burner [43]

2.3.2 Flamelet Generated Manifold (FGM)

In this work, Flamelet Generated Manifold (FGM) model is employed to model combustion. This model was first proposed by J.A. Van Oijen and L.P.H. De Goeij in 2000[44] and it is specifically designed to model Partially Premixed combustion processes, making it the most suitable for this work. This method can be seen as a merge of two classical approaches to perform simpler flame calculation: flamelet and a manifold method.

FGM model is based on a fundamental hypothesis as other manifold methods. This is the fact that it's possible to consider a multi-dimensional flame as a group of mono-dimensional flames whose chemical composition are used to build the manifold. The application of the FGM model is made in 3 separate steps:

1. Computing and solving Flamelets;
2. Store the flamelets and other parameters in a table;

3. Calculating the Probability Density Function (PDF).

The process of computing Flamelets is based on the laminar flamelet model proposed by Peters in 1984[45]. In this work, both premixed and diffusive flamelets are tested, and the results are compared. The following mathematical model is valid for Diffusive flamelets, as Premixed flamelets are similar and not discussed. This model assumes equal diffusivity of heat and all species, and 2 main equations are solved, one for the species mass fraction Y_k and one for the temperature T [46]:

$$\rho \frac{\partial Y_k}{\partial t} = \frac{1}{2} \rho \chi \frac{\partial^2 Y_k}{\partial Z^2} + S_k \quad (2.49)$$

$$\rho \frac{\partial T}{\partial t} = \frac{1}{2} \rho \chi \frac{\partial^2 T}{\partial Z^2} - \frac{1}{c_p} \sum_k H_k S_k + \frac{1}{2c_p} \rho \chi \left[\frac{\partial c_p}{\partial Z} + \sum_k c_{p,k} \frac{\partial Y_k}{\partial Z} \right] \frac{\partial T}{\partial Z} \quad (2.50)$$

where Z is the mixture fraction, ρ , $c_{p,k}$ and c_p are respectively the density, the specific heat of the k^{th} species and the mixture-averaged specific heat. H_k and S_k are the k^{th} entalpy and the source term(it can be modeled with the Arrhenius law). χ is the scalar dissipation rate and it basically expresses how the flame stretches. It is defined as follows:

$$\chi = 2D|\nabla Z|^2 \quad (2.51)$$

where D is the diffusion coefficient. χ also represents how much the chemistry is near equilibrium conditions (near 0 means equilibrium, near 1 means quenching). In the laminar flamelet model, the steady solution of equations (2.49) and (2.50) is computed. In order to create the library with the flamelet properties, $N + 1$ ode equations are solved for M different scalar dissipation rates, from 0 to its higher value.

The interaction between chemistry and turbulence is modeled with a probability density function (PDF) of Z and χ . The PDF defines the probability to find a certain variable in an infinitely small time interval. Mean value of species mass

fraction or any other arbitrary values ϕ is calculated as follows:

$$\bar{\phi} = \int_0^\infty \int_0^1 \phi(Z, \chi_{st}) P(Z, \chi_{st}) dZ d\chi_{st} \quad (2.52)$$

where χ_{st} is the stoichiometric scalar dissipation rate (when $Z = Z_{st}$) and P is the joint-PDF which can be simplified assuming that Z and χ_{st} are statistically independent so that it results in $P(Z, \chi_{st}) = P(Z) \cdot P(\chi_{st})$. The shape of each independent PDF is presumed, so that it's not very computational expensive to solve them. For the mixture fraction a β shape is usually chosen, while for χ_{st} , fluctuations are neglected, so it's modeled as Dirac delta function. To calculate the latter, the mean value of the stoichiometric scalar dissipation rate $\overline{\chi_{st}}$ is required:

$$\overline{\chi_{st}} = \frac{C_\chi \epsilon \overline{Z'^2}}{k} \quad (2.53)$$

where k and ϵ are given from the turbulence model, while $C_\chi = 2$. $\overline{Z'^2}$ is the variance of the mixture fraction. In ANSYS Fluent, transport equations for \overline{Z} and $\overline{Z'^2}$ are solved to model $P(Z)$ and thus modeling the β shape of the PDF.

Afterwards, the integration process starts for different values of \overline{Z} , $\overline{Z'^2}$ and χ_{st} and the obtained results of mean temperature and mean species fraction are stored in a table. These are called **flamelets**, and are calculated and stored before running the actual CFD code, in order to lower computational costs. However, the weak side of the laminar flamelets approach is that it is parametrized by strain (the χ variable) and thus the chemistry tends to equilibrium as the strain rate gets lower towards the outlet. The FGM model solves this problem by parametrizing the flamelet variables by the reaction progress, so that flame quenching can be appropriately modeled. The model combines two different flamelet libraries: the steady flamelet library and the unsteady one[46]. A similar procedure to the previous one is followed to build the unsteady flamelet library. The **reaction progress variable** is a scalar quantity and can be defined in many ways, in Fluent the following definition is

used:

$$c = \frac{\sum_k \alpha_k (Y_k - Y_k^u)}{\sum_k \alpha_k (Y_k^{eq} - Y_k^u)} = \frac{Y_c}{Y_c^{eq}} \quad (2.54)$$

where the superscripts u means unburnt reactant, and Y_k is the k^{th} species mass fraction. The progress variable is $c = 0$ with fresh mixture ahead of the flame and $c = 1$ with completely burnt gases behind the flame. The mean value of this variable can be extrapolated as before with a PDF approach, assuming a β shape of the function. Through (2.55) it's possible to calculate the mean progress variable \bar{c} and the progress variable variance \bar{c}^2 .

$$\bar{\phi} = \int_0^1 \int_0^1 \phi(Z, c) P(Z) P(c) dZ dc \quad (2.55)$$

The table with 4 independent variables \bar{Z} , \bar{Z}^2 , \bar{c} and \bar{c}^2 is created and stored. However, this table is only valid for adiabatic processes. For non-adiabatic flamelets, enthalpy is needed as additional parameter. Flamelet are again calculated for a range of mean enthalpy gain/loss and stored. The resulting PDF is showed in Figure (2.10).

Finally, when the CFD code runs, and the flamelet generated manifold model is enabled, it solves a transport equation for the un-normalized progress variable, which according to (2.54) is Y_c and not c . This choice has different reasons, but the main one is because according to Bray *et al.*[47] the disadvantage in using the progress variable c is that three additional scalar dissipation term have to be modeled to correctly analyze partially premixed combustion. The transport equation for Y_c is[48]:

$$\frac{\partial(\rho Y_c)}{\partial t} + \nabla \cdot (\rho \bar{v} Y_c) = \nabla \cdot \left[\left(\frac{k}{C_p} + \frac{\mu_t}{S_{c_t}} \right) \nabla Y_c \right] + \bar{S}_{Y_c} \quad (2.56)$$

where k is the laminar thermal conductivity of the mixture, μ_t is the turbulent

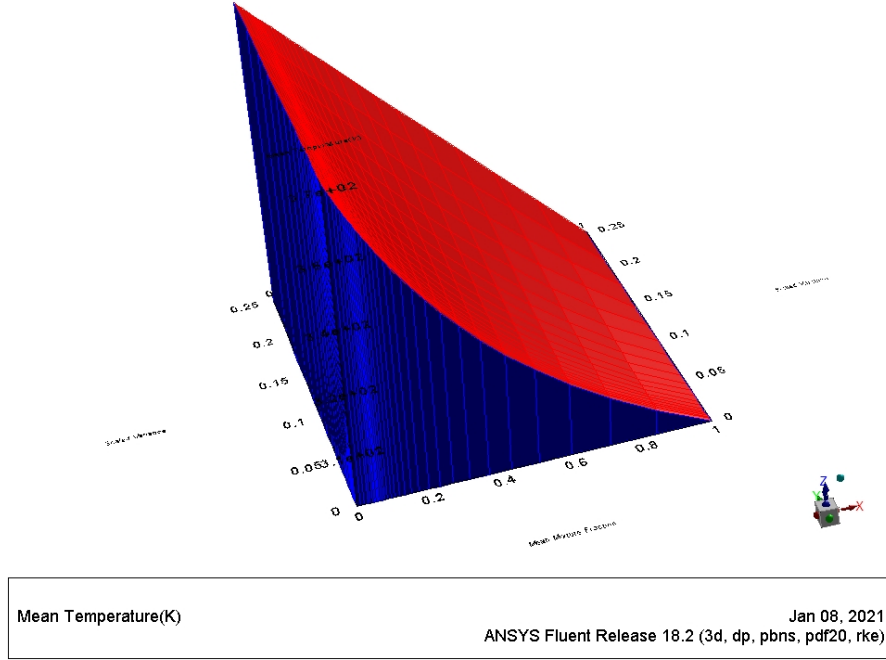


Figure 2.10: Probability Density Function (PDF)

viscosity and S_{c_t} is the turbulent Schmidt number=0.7. \bar{S}_{Y_c} is the mean source term and the FGM models it as:

$$\bar{S}_{Y_c} = \bar{\rho} \int \int S_{FR,Y_c}(c, Z) P(c, Z) dc dZ \quad (2.57)$$

where $P(c, Z)$ is the joint PDF of reaction progress and mixture fraction, while S_{FR,Y_c} is the source term of the Finite-Rate flamelet which is picked from the library built before. c and Z are assumed to be statistically independent, so the term $P(c, Z)$ in (2.57) is supposed to be the product of two beta shape PDFs. These beta functions requires variances to be solved, so another transport equation for the un-normalized reaction progress is solved to model its variance[48]:

$$\frac{\partial(\rho \bar{Y}_c'^2)}{\partial t} + \nabla \cdot (\rho \bar{v} \bar{Y}_c'^2) = \nabla \cdot \left[\left(\frac{k}{C_p} + \frac{\mu_t}{S_{c_t}} \right) \nabla \bar{Y}_c'^2 \right] + c_\varphi \frac{\mu_t}{S_{c_t}} |\nabla \bar{Y}_c|^2 - \frac{\rho c_\varphi}{\tau_{turb}} \bar{Y}_c'^2 \quad (2.58)$$

where $c_\varphi = 2$.

2.3.3 Species and reactions

A model with 20 species and 82 reactions is used. The model is taken from the ANSYS lecture input file for combustion simulations, which have been generated by the software CHEMKIN. The list of species contained in the model is in Table 2.4.

CH ₄	O ₂	CO ₂	CO	H ₂ O	H ₂	H	O	OH	HO ₂
CH ₂	CH _{2(s)}	CH ₃	HCO	CH ₂ O	CH ₃ O	C ₂ H ₄	C ₂ H ₅	C ₂ H ₆	N ₂

Table 2.4: Species employed in the combustion model

2.4 User defined Functions

In this work, some User Defined Functions (UDF) are employed to model flame structure closer to reality. The UDF involved modified two important parameters for flame definition: the laminar flame speed and the critical strain rate. These parameters are introduced and discussed in the following sections.

2.4.1 Laminar flame speed

The laminar flame speed is defined as the speed at which a flame propagates through a homogeneous and resting mixture of fuel and oxidizer, in adiabatic conditions[49]. The simplest case is when the flame is perpendicular to the flame front, but generally, the flow approaches the flame with an angle, as showed in Figure 2.11:

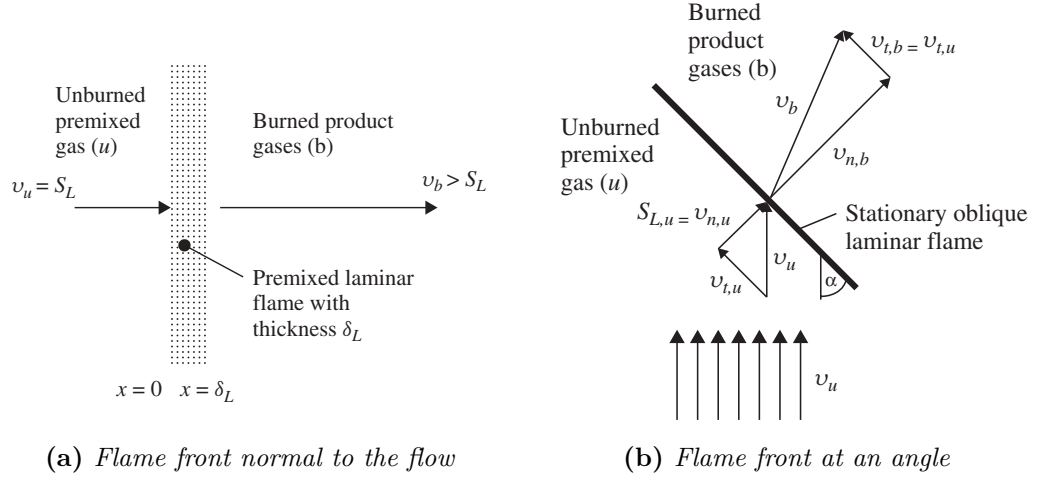


Figure 2.11: Visualization of laminar flame speed[50]

After being burnt, the mixture increases significantly its temperature, thus its density drops. The continuity equation must be satisfied so the velocity of the burnt gases must be higher than the laminar flame speed S_L . The laminar flame speed depends on some characteristic parameters, which are the excess fuel factor φ , pressure, temperature and the type of fuel:

$$S_L = f(\varphi, p, T, fuel)$$

Some empirical formulas have been developed during the years to model this quantity. One of those is from the work of Göttgens *et al.*[51]:

$$S_L = FY_{f,u}^m \exp\left(-\frac{G}{T_0}\right) \left(\frac{T_b - T_0}{T_b - T_f}\right)^n \quad (2.59)$$

where:

- $Y_{f,u}^m$ is the mass fraction of fuel in the unburnt gas;
- T_0 is the inner layer temperature of the laminar flame;
- T_u is the temperature of the unburnt mixture;

- T_b is the equilibrium temperature of burnt products;
- F, G, m, n are empirically determined coefficients.

For methane CH_4 the letters were determined and showed in Table 2.5:

Fuel	F	G	m	n
CH ₄	22.176	-6444,3	0.5651	2.5158

Table 2.5: Coefficients of eq.(2.59) [51]

However, the most common empirical expression of the laminar flame speed S_L is the one found by Metghalchi *et al.*[52]:

$$S_L = S_{L0} \left(\frac{T_u}{T_0} \right)^\gamma \left(\frac{P_u}{P_0} \right)^\beta \quad (2.60)$$

where T_u and P_u are respectively the temperature and pressure of the fresh mixture, γ is a thermal exponent and β is a barometric one. T_0 and P_0 are a reference temperature and pressure. This expression for the laminar flame speed allows to take into account the increase in temperature and pressure that features the modern gas turbine engines. Within the proposal for the laminar flame speed expression, the value of S_{L0} was modeled as[52]:

$$S_{L0} = C_1 + C_2(\varphi - C_3)^2$$

where φ is excess of fuel coefficient, while C_1, C_2 and C_3 are coefficients depending on fuel. γ and β are modeled as:

$$\begin{aligned} \gamma &= 2.18 - 0.8(\varphi - 1) \\ \beta &= -0.16 + 0.22(\varphi - 1) \end{aligned}$$

However, Lukachev *et al.* in his work[53] analyzed many empirical and experimental

works on previous modeling of laminar flame speed. He claimed 3 major results:

1. Equation 2.59 overestimates the value of laminar flame speed when $\varphi > 1$;
2. Equation 2.60 can only be used for fuel pressures below 0.2 MPa, because above that the it overestimates the laminar flame speed;
3. The GRI 3.0 mechanism well fit the experimental data, making it a good candidate for computing the laminar flame speed in every operating conditions.

Within these statements, Lukachev *et al.* used the curve fitting toolbox from the MATLAB environment to improve the coefficients of eq.(2.60). Their results showed the following relation:

$$S_{L0} = 145\varphi^3 - 850\varphi^2 + 1265\varphi - 325 \quad (2.61)$$

$$\gamma = \gamma_1\varphi^2 + \gamma_2\varphi + \gamma_3 \quad (2.62)$$

$$\beta = \beta_1\varphi^2 + \beta_2\varphi + \beta_3 \quad (2.63)$$

where the unknown coefficients of these curves are:

γ_1	γ_2	γ_3	β_1	β_2	β_3
7.6	-10.8	5.1	-0.966	1.1	-0.4715

Table 2.6: Coefficients of equations (2.62, 2.63)

Figure 2.12 shows the laminar flame speed obtained with the formula proposed by Lukachev, with $T_u = T_0 = 800K$ and $P_u = P_0 = 101325Pa$:

As clear from the figure, there are some ranges of φ where the laminar flame speed is negative. Physically, this is not possible, and it means that combustion does not occur. In order to take this into account, laminar flame speed was set to 0 when $\varphi < 0.33$ and $\varphi > 1.9$. In Figures 2.13 it is showed the dependence of the laminar flame speed on pressure, temperature and φ .

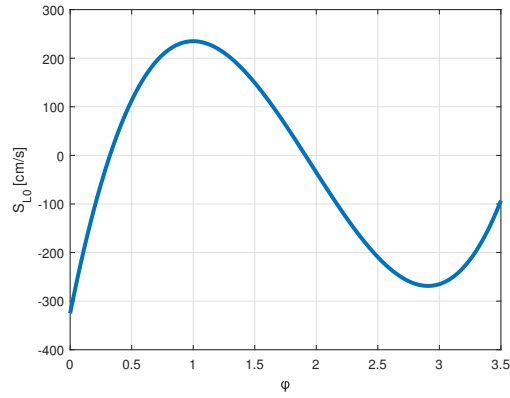


Figure 2.12: Laminar flame speed with $T_u = 800K$ and $P_u = 101325Pa$

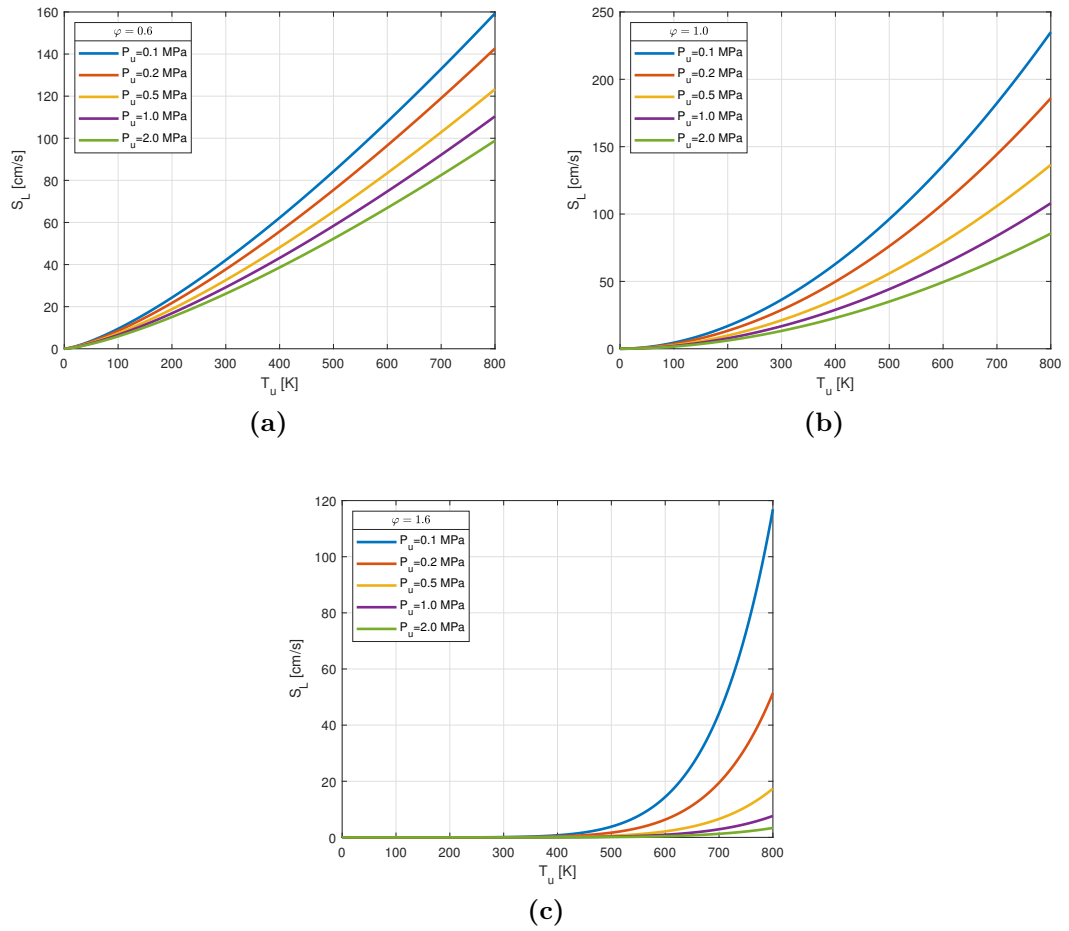


Figure 2.13: Laminar flame speed's dependence on pressure, temperature and φ

The present work is based on the relation of laminar flame speed presented by Lukachev *et al.*. A UDF was created using the programming language C and used in this work. A detailed description of the script for computing the laminar flame speed is shown below.

Laminar_flame_speed

```

1 DEFINE_PROPERTY(user_LaminarFlameSpeed, cell, thread)
2 {
3     real fi, sl, z, Pk, Tk, Tt, Tv, S10, T, P, ST, SP;
4
5     /*Section 1 */
6     Pk = 104365;
7     Tt = 288;
8     Tv = 373;
9     z = C_FMEAN(cell, thread);
10    Tk = Tv - z*(Tv - Tt);
11    P = Pk / 101325;
12    T = Tk / 800;
13
14    /*Section 2 */
15    {if (0.005767 > z)
16        sl = 0;
17    else if (z > 0.1620207)
18        sl = 0;
19    else
20
21    /*Section 3 */
22        fi = (17.24*z) / (1 - z);
23        ST = 7.6 - 10.8*fi + 5.1*pow(fi, 2);
24        SP = -0.966 + 1.1*fi - 0.4715*pow(fi, 2);
25        S10 = 145 * pow(fi, 3) - 850 * pow(fi, 2) + 1265 * fi - 325;
26        sl = 0.01*pow(T, ST)*pow(P, SP)*S10;
27    }
28    return sl;
29 }

```

The script is divided into 3 main sections, which are highlighted in the script itself:

- **Section 1:** the temperature of both fuel and air and the pressure in the combustion chamber are set. A detailed description of these values is available in Chapter 3;
- **Section 2:** as discussed and shown in Figure 2.12, laminar flame speed is set to 0 in a certain range of φ , otherwise it would be negative thus no combustion occurs at all.
- **Section 3:** laminar flame speed is calculated using the equation 2.60 and the coefficients given by Lukachev's work[53].

2.4.2 Critical strain rate

It has been showed how operating combustors near lean blowout has a great effect on the heat release of the mixture. This is due to the significant stretch that the flame experiences in lean conditions. To take this stretch into account, the source term in the transport equation of the progress variable is multiplied by a new factor, called *stretch factor* G [54]. It physically represents the probability of flame quenching. If the flame is not stretched, $G = 1$ and it won't quench as its probability is 0%. The stretch factor is defined as[54]:

$$G = \frac{1}{2} \operatorname{erfc} \left\{ -\sqrt{\frac{1}{2\sigma}} \left[\ln \left(\frac{\epsilon_{cr}}{\epsilon} \right) + \frac{\sigma}{2} \right] \right\} \quad (2.64)$$

where

- erfc is the complementary error function;
- σ is the standard deviation of the ϵ distribution

$$\sigma = \mu_{str} \ln \left(\frac{L}{\eta} \right) \quad (2.65)$$

with $\mu_{str} = 0.26$ is a coefficient for dissipation pulsation, L is the turbulent length scale and η is the Kolmogorov micro-scale;

- ϵ_{cr} is the turbulent dissipation rate at the critical strain rate and it is defined as

$$\epsilon_{cr} = 15\nu g_{cr}^2 \quad (2.66)$$

with ν cinematic viscosity and g_{cr} the critical strain rate.

Normally, g_{cr} is set with 1×10^8 so the flame doesn't stretch. In order to take flame stretching into account, Zimont[54] suggest some adjustment based on experimental data, so that an appropriate value can be set. This parameter can be set as:

$$g_{cr} = \frac{BS_L}{\alpha} \quad (2.67)$$

where $B = \text{const} = 0.5$, S_L is the laminar flame speed introduced in (2.59) and α is the thermal diffusivity of the unburnt mixture. It is defined as:

$$\alpha = \frac{\lambda_k}{C_p \rho_k} \quad (2.68)$$

where λ_k and ρ_k are respectively the thermal conductivity and the density of the PDF mixture (air+fuel) and C_p is the specific heat at constant pressure. Such dependency of the critical strain rate on the laminar flame speed is neglected by Fluent, and it can only be implemented using a User Defined Function. Like for laminar flame speed, a UDF was created using the programming language C and used in this work. A detailed description of the script for computing the critical strain rate is shown below.

Critical_strain_rate

```

1 DEFINE_PROPERTY(user_Critical_Strain_Rate, cell, thread)
2 {
3     real z, g, S1, a, Cp, CpCH4, CpO2, CpN2, Cpt, Cpv, la, laCH4, laO2,
4     laN2, lav, lat, ro, roCH4, roO2, roN2, rot, rov, Tt, Tv, Tk, Pk, RCH4, Rv, rCH4
5     , muCH4, muv, mut;
6
7     /*Section 1*/
8     z = C_FMEAN(cell, thread);
9     Pk = 104365;
10    Tt = 288;
11    Tv = 373;
12    Tk = Tv - z*(Tv - Tt);
13    rCH4 = (60 * pow(z, 2)) / (76 * pow(z, 2) - 32 * z + 16);
14    S1 = C_LAM_FLAME_SPEED(cell, thread);
15
16    /*Section 2*/
17    laO2 = 3.4605*pow(10, -3) + 7.8176*pow(10, -5)*Tk - 1.0680*pow
18    (10, -8)*pow(Tk, 2);
19    laN2 = 8.4243*pow(10, -3) + 6.1654*pow(10, -5)*Tk - 4.4972*pow
20    (10, -9)*pow(Tk, 2);
21    lav = laO2*0.21 + laN2*0.79;
22    Rv = 287.1;
23    rov = Pk / (Rv*Tk);
24    CpO2 = 834.8265 + 0.292958*Tk - 0.0001495637*pow(Tk, 2) +
25    3.413885*pow(10, -7)*pow(Tk, 3) - 2.278358*pow(10, -10)*pow(Tk, 4)
26    ;
27    CpN2 = 979.043 + 0.4179639*Tk - 0.001176279*pow(Tk, 2) +
28    1.674394*pow(10, -6)*pow(Tk, 3) - 7.256297*pow(10, -10)*pow(Tk, 4)
29    ;
30    Cpv = 0.21*CpO2 + 0.79*CpN2;
31
32    /*Section 3*/
33    laCH4 = -3.7173*pow(10, -2) + 1.0376*pow(10, -4)*Tk + 7.3734*pow
34    (10, -8)*pow(Tk, 2);

```

```

26 RCH4 = 530;
27 roCH4 = Pk / (RCH4*Tk);
28 CpCH4 = 403.5847 + 9.057335*Tk - 0.01442509*pow(Tk, 2) +
1.580519*pow(10, -5)*pow(Tk, 3) - 6.343051*pow(10, -9)*pow(Tk, 4);
29
30 /*Section 4*/
31 lat = laCH4;
32 la = lat*rCH4+lav*(1- rCH4);
33
34 rot = roCH4;
35 ro = rot*z+rov*(1-z);
36
37 Cpt = CpCH4;
38 Cp = Cpt*z+Cpv*(1-z);
39
40 /*Section 5*/
41 a = la / (Cp*ro);
42 g = 0.5*pow(S1, 2) / a;
43 return g;
44 }

```

The script is divided into 5 main sections, which are highlighted in the script itself:

- **Section 1:** the temperature of both fuel and air and the pressure in the combustion chamber are set. A detailed description of these values is available in Chapter 3;
- **Section 2:** the properties of air such as thermal conductivity λ and specific heat C_p are calculated using a polynomial law. These parameters depends only on the temperature of the mixture;
- **Section 3:** the same thermal parameters calculated for air are now computed for the fuel;
- **Section 4:** the thermal properties of the mixture fuel+air are calculated;

- **Section 5:** the critical strain rate g_{cr} is finally calculated using equation (2.67).

Chapter 3

Numerical and experimental setup

This section is dedicated to the presentation and the description of the combustion system object of this work. The geometry, the mesh and the boundary conditions applied to the model will be introduced and the strategy to simulate lean blowout will be discussed.

3.1 Description of the combustion chamber

The combustion chamber object of this work was modeled based on the one in the Samara National Research University. A schematic drawing is shown in Figure 3.1.

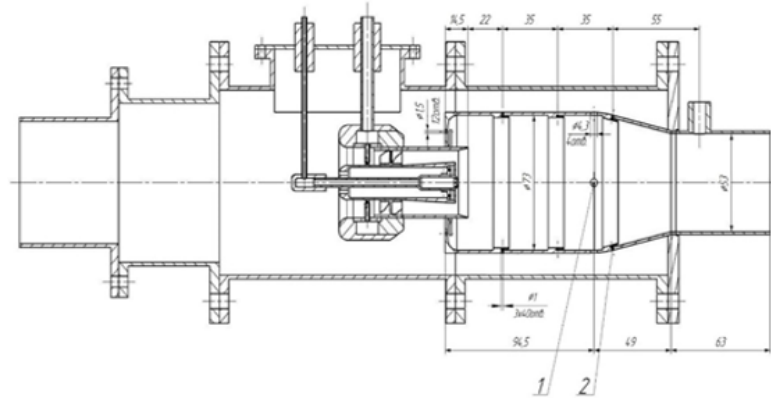


Figure 3.1: Combustion chamber

On the chamber there are three sets of holes, one of which in the conical segment, in order to prevent the main body from overheating and one set of bigger holes for dilution. Before the chamber, air is forced to pass through a swirler, which gives vorticity to the fluid, and creates a rotational bubble where air and fuel mix properly. The main feature of this combustor is that it has a pilot fuel nozzle and a main one, as shown from Figure 3.1. Fuel feed is ensured from 2 separate fuel pipes, the main fuel pipe goes into the swirler vane while pilot fuel is sprayed directly into the chamber.

3.2 Mesh

The file .msh containing the mesh of the combustion system was gently provided by Prof.Zubrilin. The mesh has 1.6 million of elements and around 350 thousand of nodes. Mesh is coarse in the part of domain which is not interested by turbulence or combustion. It is finer where reaction occurs, in the mixing region, and near the cooling and dilution holes. There is also an inflation technique near the wall to catch the effect of the boundary layer.

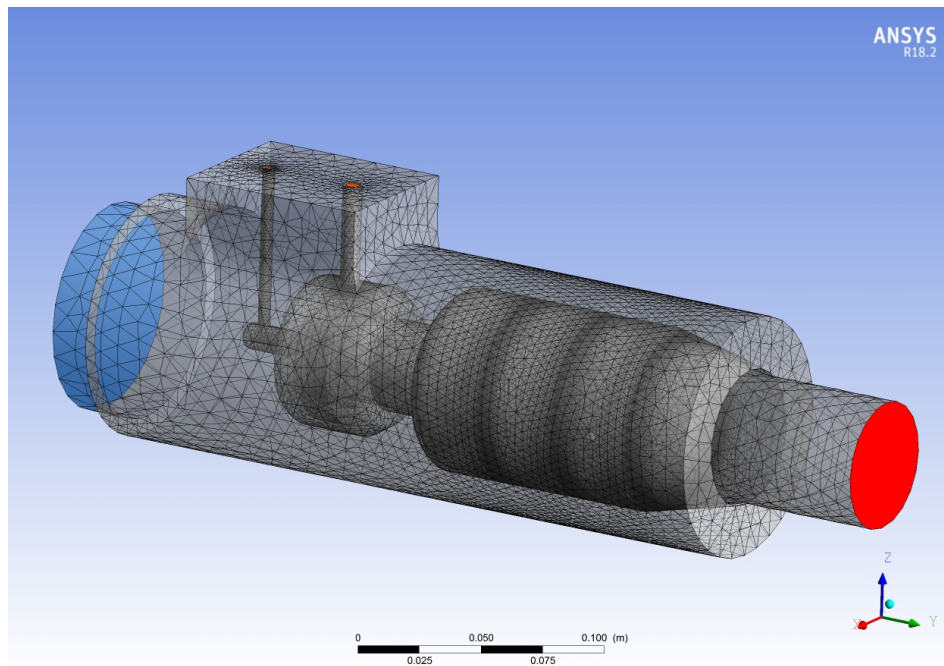


Figure 3.2: Mesh visualization

3.3 Boundary conditions

A list of the different boundary conditions is following. The **operating pressure** of all the simulations were set up to $101325 Pa$ so all the following indicated pressures are considered to be added to the atmospheric pressure.

3.3.1 Inlet

The inlet was set as **pressure inlet** with a gauge total pressure of $3040 Pa$ and a total temperature of $373 K$. This number is exactly the pressure loss expected from the chamber. However, the air mass flow rate is known as it is one of the parameters of the chosen operating point. Nevertheless, the inlet was not set up as mass flow inlet because mass flow was considered to be a check value if the simulation was run correctly.

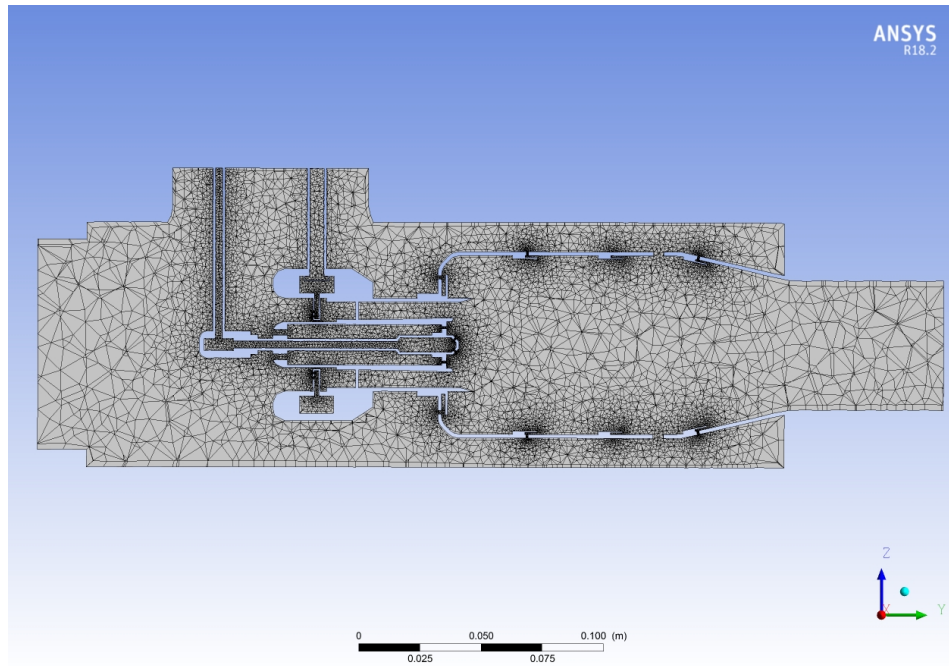


Figure 3.3: Mesh section

3.3.2 Outlet

The outlet was set as **pressure outlet** with a gauge total pressure of 0 Pa , which according to the operating conditions corresponds to the atmospheric pressure.

3.3.3 Pilot fuel and Main fuel

Both main and pilot fuel inlets were set as **mass flow inlet** with a temperature of 288 K .

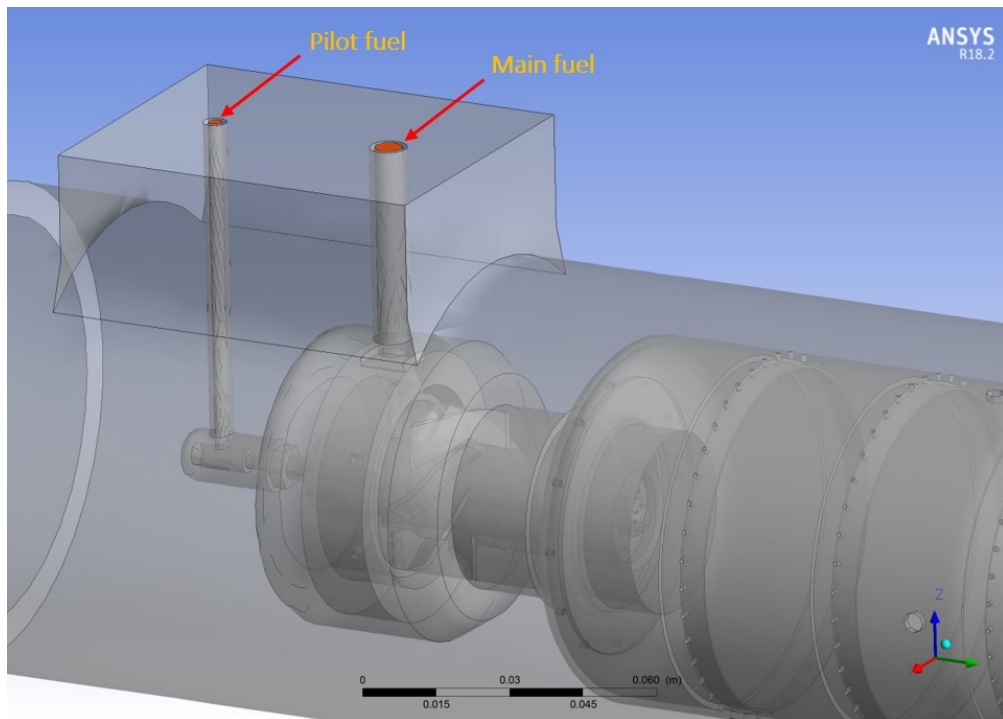


Figure 3.4: Fuel inlets

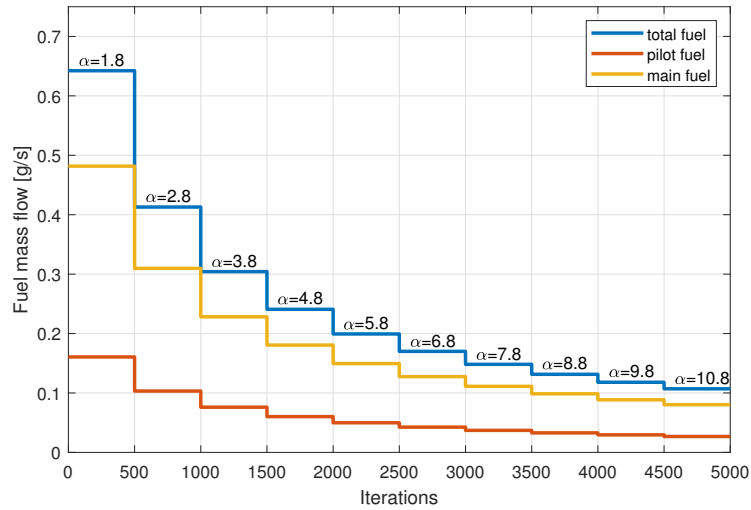
In order to catch lean blowout, the inlet supply of air was maintained constant, while the fuel mass flow was lowered. However, the existence of 2 fuel nozzles (pilot and main) implied that fuel mass flow was lowered with different fuel proportions between the 2 nozzles. In other words, 7 different cases were tested, each one with a different percentage of fuel mass flow as shown in the following table:

In each one of these points the total fuel mass flow was lowered. Starting from a condition of stable combustion, identified by the *equivalence ratio* $\alpha = 1.8$, fuel was initially lowered according to a constant step of $\alpha = 1$, bringing the equivalence ratio to 2.8, 3.8, 4.8 and so on up to 10.8.

As an example, Point 2 is analyzed. As shown by table 3.1, this point is characterized by 25% pilot fuel and 75% main fuel. The value of fuel for both pilot and main nozzles are reported in the following table.

To visualize how fuel mass flow was lowered in the simulations, it's possible to draw a chart (Figure 3.5).

	$\dot{m}_{pilot}^f / \dot{m}_{tot}^f$	$\dot{m}_{main}^f / \dot{m}_{tot}^f$
Point 1	5%	95%
Point 2	25%	75%
Point 3	50%	50%
Point 4	75%	25%
Point 5	95%	5%

Table 3.1: Fuel distribution in tested cases

Figure 3.5: Fuel lowering method for Point 2

3.4 Solution monitors set

In order to monitor combustion progress and evolution, three report files have been set for all the simulations. Thanks to these collected data, it's possible to extrapolate whether combustion in the chamber still occurs and how it evolves when fuel flow is lowered.

		Point 2			
α	$\dot{m}_{tot}^f [g/s]$	$\dot{m}_{pilot}^f / \dot{m}_{tot}^f$	$\dot{m}_{main}^f / \dot{m}_{tot}^f$	$\dot{m}_{pilot}^f [g/s]$	$\dot{m}_{main}^f [g/s]$
1.80	0.6423	25%	75%	0.1606	0.4817
2.80	0.4129	25%	75%	0.1032	0.3097
3.80	0.3042	25%	75%	0.0761	0.2282
4.80	0.2408	25%	75%	0.0602	0.1806
5.80	0.1993	25%	75%	0.0498	0.1495
6.80	0.1700	25%	75%	0.0425	0.1275
7.80	0.1482	25%	75%	0.0371	0.1112
8.80	0.1314	25%	75%	0.0328	0.0985
9.80	0.1180	25%	75%	0.0295	0.0885
10.80	0.1070	25%	75%	0.0268	0.0803

Table 3.2: Fuel values for Point 2

These three monitors are:

- **Outlet temperature:** a *facet average* of static temperature on the outlet surface was set. Static temperature is a good indicator of the presence of combustion. However, near LBO, sometimes it is not the best monitor for combustion presence;
- **Outlet mean mixture fraction:** a *area-weighted average* of mean mixture fraction was set on the outlet surface as well. The mixture is an indication of the unburnt fuel at the outlet, which designates combustion presence;
- **Outlet progress variable:** a *facet average* of the progress variable was set

on the outlet too. This indicator quantifies the combustion process, and it depends on a ratio between burnt and unburnt species.

3.5 Running the simulations

All the simulations were performed on the Supercomputer "Sergey Korolev" installed at the Supercomputing Center of the Samara University. The system provides a peak performance of 40 TFlops. Any other information about its features and hardware settings can be found on its website[55]. For each Point as defined in Table 3.1 three simulations have been run. During each simulation boundary conditions for pilot and main fuel were changed to simulate LBO. Due to the fact that the simulation were run on the cluster, a Bash script was needed to change the boundary conditions. For each simulation, a .txt file was prepared. Each point had different boundary conditions but the instructions contained in the Bash file are the same. An example of the Bash file is reported in Appendix A, and overall it has the following structure:

- **Read** the starting case and data file. This is a starting case that needs some iterations to get a steady solution;
- **Open** the User Defined Function library. This library has been previously compiled on the server, and placed in a folder called "libudf". With this instruction the library is read. Not all the simulations used UDF functions, so this instruction may not be present in some bash files;
- **Run** # iterations, which may depends on the Point tested. Some cases need more iterations get steady residuals;
- **Save** the results in a file.
- **Change** the mass flow rate of the **pilot** nozzle according to tables like Table 3.2;

- **Change** the mass flow rate of the **main** nozzle according to tables like Table 3.2;
- **Run** # iterations with the new boundary conditions for fuel;
- **Save** the results in a new file.

At the end of the simulations, a series of files will be saved as output, one for each time boundary conditions have changed. As example, the Bash file for Point 2 where UDF have been employed is showed. The value of fuel mass flow for both pilot and main fuel reflects the one in Table 3.2.

3.6 Experimental setup

Experimental measures for lean blowout was taken in 2016 at the Samara National Reasearch university. Although the focus of this work is not to explain how experimental data was taken, a brief description of the reference burner and of the experimentally test bench is provided in this section.

The reference burner object of this work is shown in Figure 3.6. The pictures show only the burner, not the whole combustion chamber. The flame tube, which should be attached to the burner is in fact absent. It is worth noting how the burner is composed: starting from Figure 3.6a the swirler inside the burner is visible, this is the inlet of the chamber, where the hot air comes in. On Figure 3.6b the side view of the burner is shown. Here the pipes of pilot fuel and main fuel are clearly visible, as the length of the burner itself. In the end, in Figure 3.6c, the nozzles of the pilot fuel are visible, while the ones of the main fuel are hidden inside, before the swirler. A view of the experimental setup is shown in Figure 3.7. Here the two circuits of both pilot fuel and main fuel are clearly shown. Each pipe has a pressure gauge right before the chamber and there are also two flowmeters, one for the total mass flow rate of fuel on the left, and one for the main fuel pipe, which is the one on top in the Figure. There is also a ball valve on the main fuel circuit, which was set to be open only to ignite the chamber when additional fuel was needed.



(a)

(b)



(c)

Figure 3.6: Burner

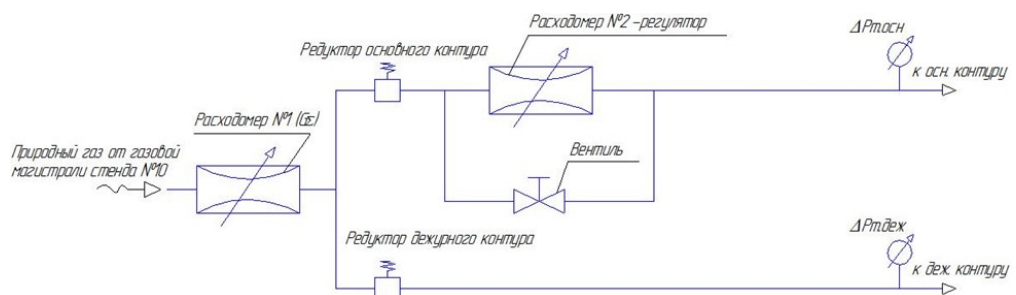


Figure 3.7: Experimental setup

Chapter 4

Results

Aim of this chapter is to show the results obtained, both numerical with ANSYS Fluent and experimental with a reference combustor. Results will be introduced, compared and discussed.

4.1 Numerical results

Scope of this section is to show the results obtained for all the cases that were investigated. Numerical simulations were performed with ANSYS Fluent and the outcomes are showed and discussed in the following sections. Every section corresponds to a different turbulence model used. Before LBO analysis, some 3D results have been collected to make sure that the flow streamlines goes according to predictions. In the next Figure, some streamlines are showed, from inlet air to both main and pilot fuel: About Figure 4.1 it's worth noting how the flow is put into rotation thanks to the swirler. A big recirculation zone is formed inside the chamber, and this enhances mixing of fuel and air. A small fraction of air surrounds the chamber and goes into the holes around it, cooling its wall and diluting the burnt mixture. In Figure 4.2 streamlines for both pilot and main fuel are showed. As seen in Figure 4.2a, main fuel is injected before the swirler, which

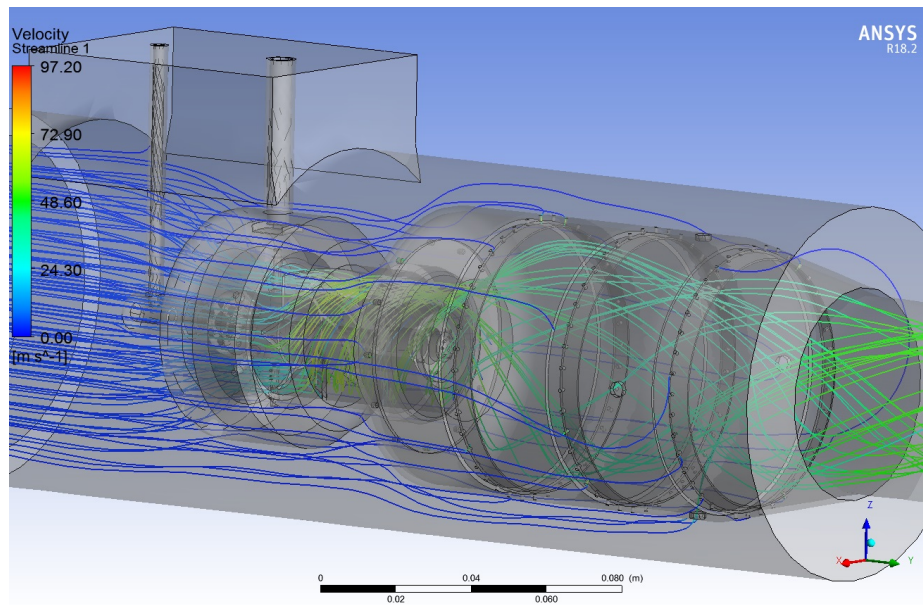
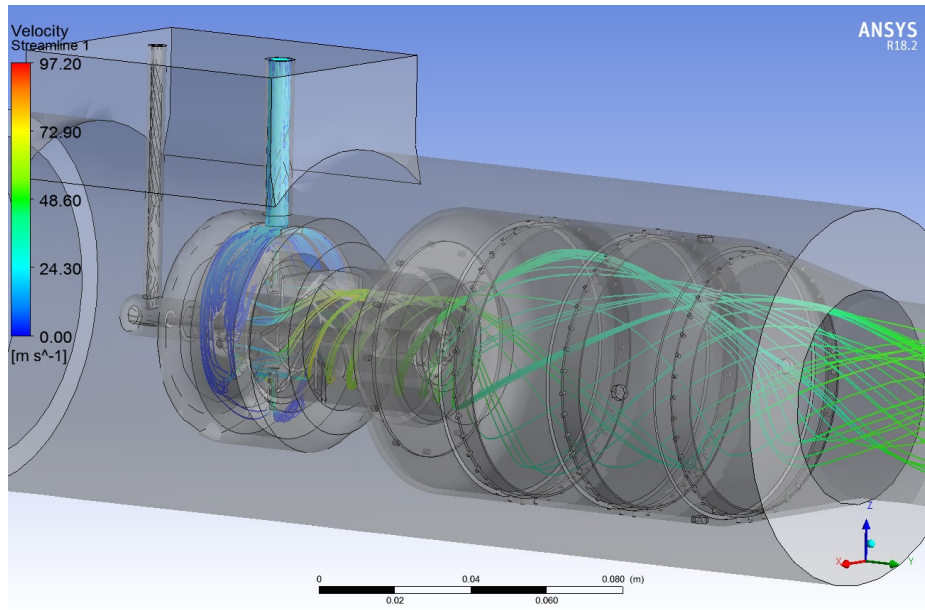
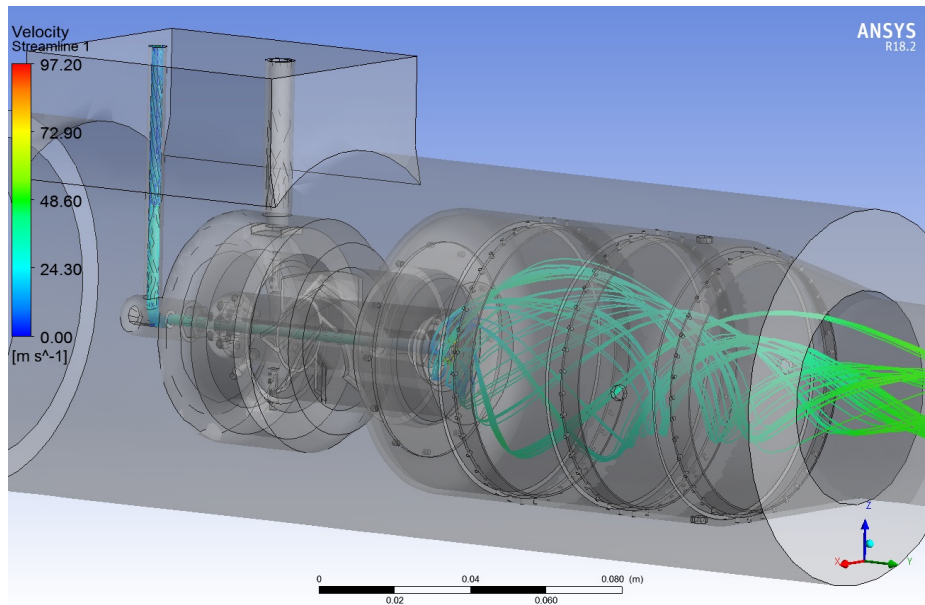


Figure 4.1: Inlet flow streamlines

gives vorticity to the flow of both main fuel and air before the combustion chamber. It is clear how main fuel is premixed with the air while in the swirler. A different case is Figure 4.2b, where streamlines for pilot fuel are showed. Here, it's clear how the pilot flame is a diffusive one, because it is directly injected in the combustion chamber and then it starts rotating with the surrounding flow in the recirculation zone.



(a) *Main fuel streamlines*

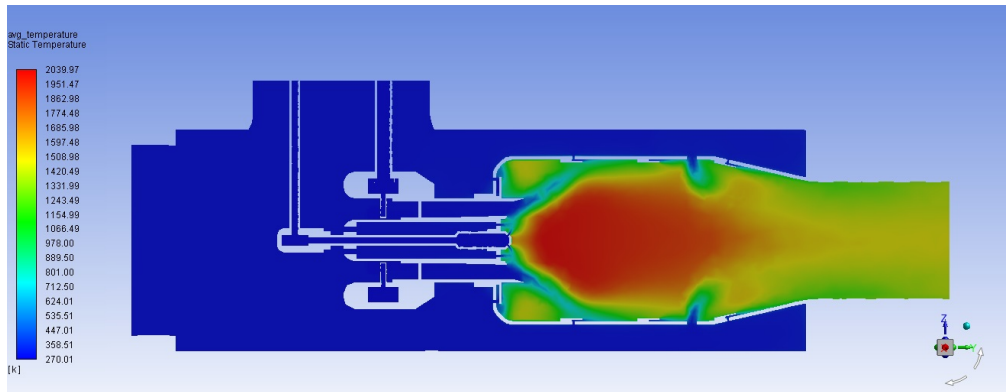


(b) *Pilot fuel streamlines*

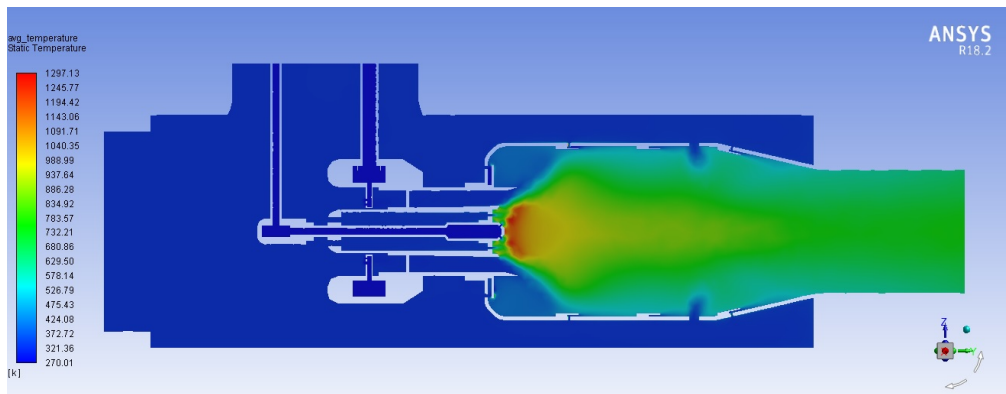
Figure 4.2: Streamlines for main and pilot fuel

4.1.1 Realizable $k - \epsilon$ model

The first turbulence model used is the Realizable $k - \epsilon$. As said in section 1.2.2, the first simulation run was to establish a point of stable combustion. For this purpose $\alpha = 1.8$ was chosen as starting point, then fuel mass flow was lowered. Contours of the most noteworthy variables were printed in Fluent. Temperature and velocity were monitored, but also progress variable, which is a great indicator of flame stability. The first case showed in this section is the one denoted by Point 2, where pilot fuel is 25% and main fuel is 75% of the total inlet fuel as described in Table 3.2. For this particular point, lean blowout was found at $\alpha = 4.305$, so the variables monitored will be compared between $\alpha = 1.8$ and $\alpha = 4.30$ (just prior to LBO). In the next figures, contours of these 3 variables are showed: The static temperature at stable combustion is very high, around 2000K and the region in which this temperature is reached is quite large, as showed in Figure 4.3a. On the other hand, near LBO the flame is only in a small region in the primary zone and in its highest point, the temperature reaches 1553K, as showed in Figure 4.3b. Contours of velocity are showed in Figure 4.4:



(a) Contour of static temperature - $\alpha = 1.80$ - Point 2

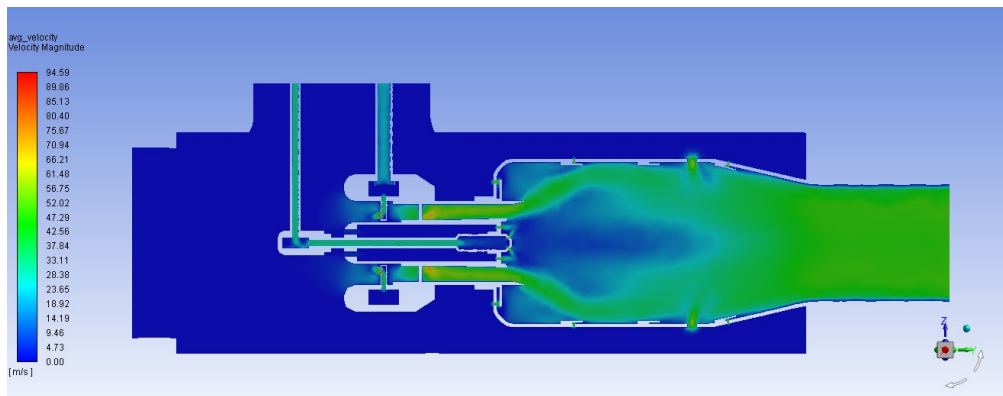


(b) Contour of static temperature - $\alpha = 4.30$ - Point 2

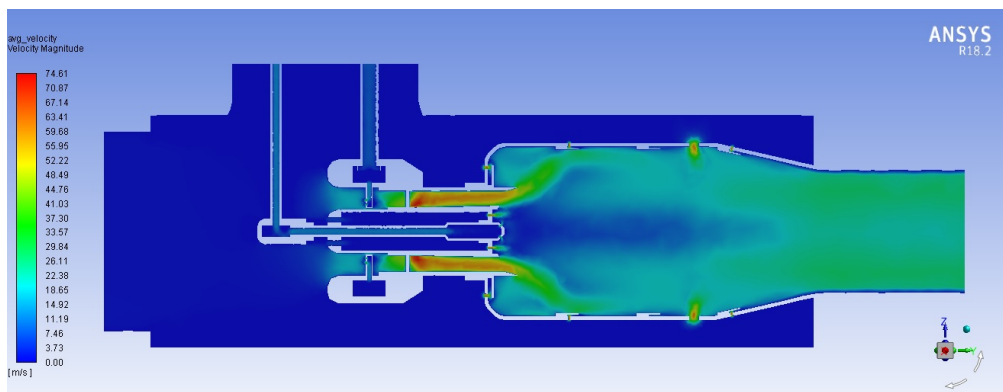
Figure 4.3: Contour of static temperature at stable combustion and near LBO

In these contours, it is clear how the recirculation zone is formed ahead of the fuel injectors. This zone guarantees a good mixing between chemical species and gives to the fluid enough residence time to complete its reactions. The swirler gives vorticity to the fluid thus creating a recirculation region in the chamber. The velocity pattern in both $\alpha = 1.80$ and $\alpha = 4.30$ looks pretty much the same, but the velocity in the first condition is slightly higher, because of the higher mass flow of fluid involved (air+fuel).

Contours of the progress variable are showed in Figure 4.5:



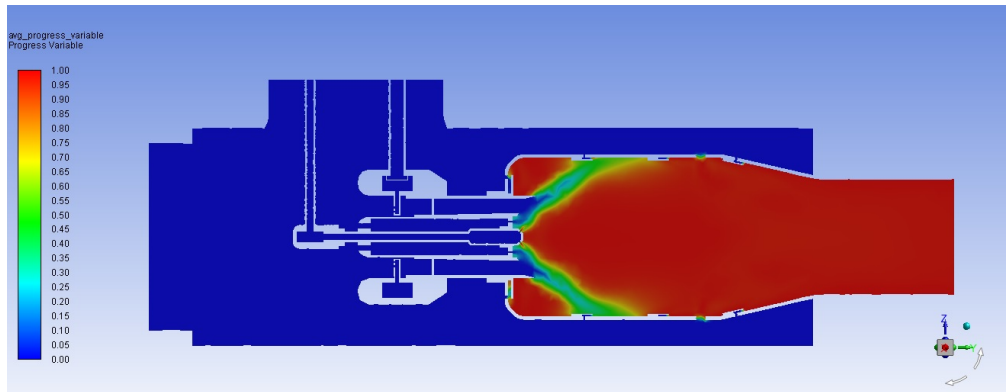
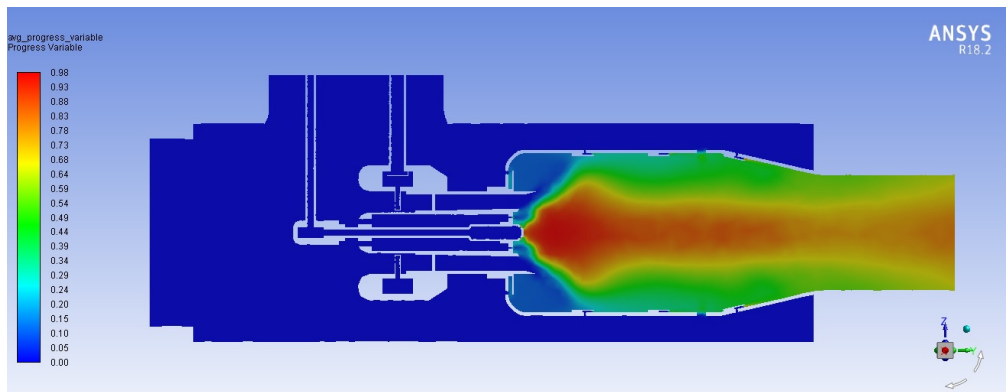
(a) Contour of velocity - $\alpha = 1.80$ - Point 2



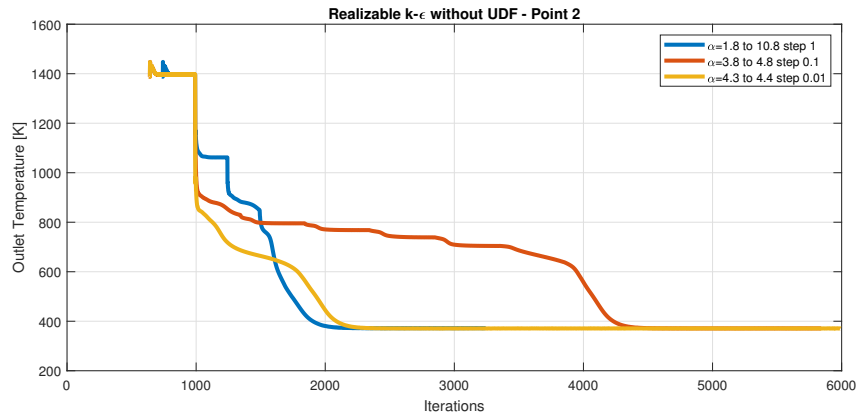
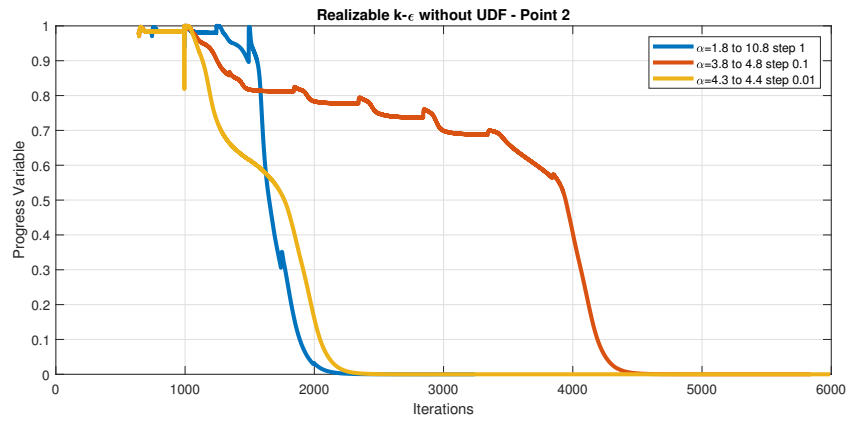
(b) Contour of velocity - $\alpha = 4.30$ - Point 2

Figure 4.4: Contour of velocity at stable combustion and near LBO

Based on its definition, the progress variable expresses is and how the mixture is burned. It is 1 when the mixture has completely burned, otherwise not. From Figure 4.5a it's possible to notice how combustion is fully developed because the progress variable is equal to 1 in most part of the chamber. A different situation is near LBO in Figure 4.5b. Here the progress variable seriously decreased, indicating a less stable flame which is about to quench. Following, graphs with the outlet temperature and the progress variable are presented and discussed:

(a) Contour of progress variable - $\alpha = 1.80$ - Point 2(b) Contour of progress variable - $\alpha = 4.30$ - Point 2**Figure 4.5:** Contour of progress variable at stable combustion and near LBO

In Figure 4.6a, the graph of the evolution of temperature in the simulation is showed. For Point 2, three simulation have been run. In the first, denoted with a blue line, the fuel mass flow rate was decreased in terms of α from 1.8 to 10.8 with a step of 1. Once blowout was found between 3.8 and 4.8, a second, more precise simulation was launched. This time from 3.8 to 4.8 with step 0.1. Here, blowout was found at $\alpha = 4.3$. The third, last, simulation was launched between 4.3 and 4.4 with step 0.01. Here, blowout was found at $\alpha = 4.31$. So the real blowout is between $\alpha = 4.30$ and $\alpha = 4.31$. Blowout for this case is declared to be at $\alpha = 4.05$, since it is the middle value between the latters. From the graph with a step high enough, it's possible to notice the moment where boundary conditions

(a) *Temperature*(b) *Progress Variable***Figure 4.6:** Temperature and Progress variable evolution during simulation

(in terms of fuel mass flow rate) changes. Temperature and progress variable drop when this happens, and when they reach 373K and 0 respectively, there the flame has quenched. Overall, the analysis of all the points with different combinations of pilot and main fuel as described in section 3.3.3 has led to different values of lean blowout. These data are showed in the following graph:

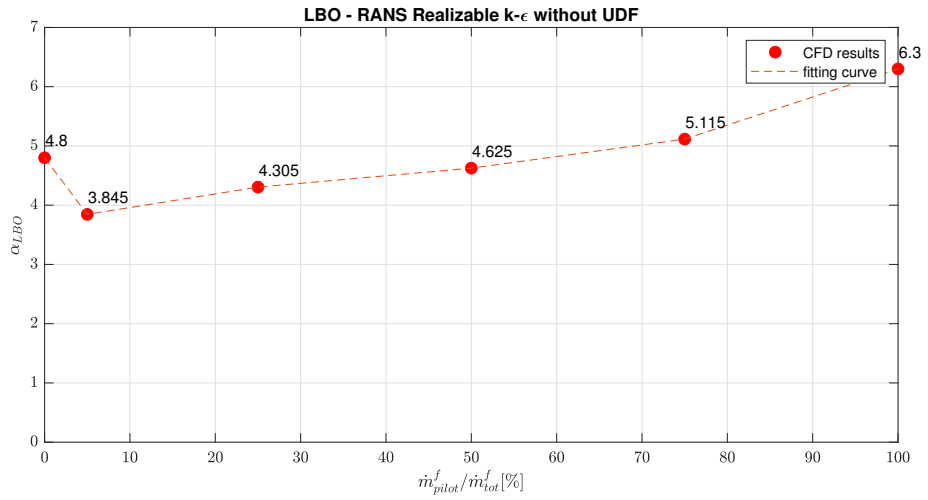


Figure 4.7: Lean Blowout results for Realizable $k - \epsilon$ model without UDF

The results for the Realizable $k - \epsilon$ model without UDF show that overall the blowout resistance grows with the amount of fuel delivered by the pilot nozzle.

4.1.2 Reynolds Stress Model

In this section, results gathered with the Reynolds Stress model (RSM) will be showed. The first case showed in this section is the one denoted by Point 3, where both pilot and main fuel are 50% of the total inlet fuel as described in Table 3.2. For this specific point, lean blowout was found to be at $\alpha = 5.055$. The contour at $\alpha = 1.8$ where combustion is stable are not showed, since there are no main differences from the $k - \epsilon$ one, and since they have been already presented and discussed. For the same reason, the velocity contour will be omitted too. The monitored variables will be showed just before LBO at $\alpha = 5.05$:

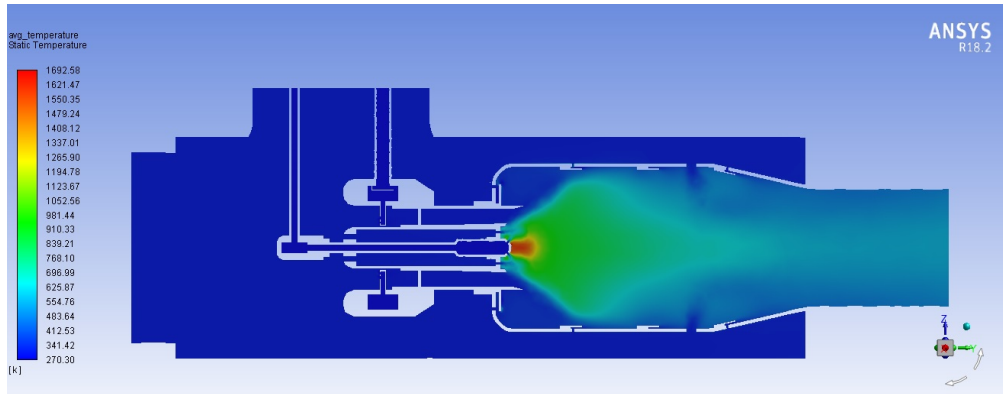


Figure 4.8: Contour of Temperature - $\alpha = 5.05$ - Point 3

In Figure 4.8, the contour of temperature prior to LBO is slightly different from the one found with the Realizable $k - \epsilon$ model in Figure 4.3b. With the RSM the high temperature region, denoted with a bright red colour, is larger than with the previous model, probably because of the higher accuracy in modeling turbulence of the RSM model, which results in higher mixing of the species and better combustion of the latters. Moreover, because of the same reason, the flame has a higher maximum temperature, which reaches around 1721K, 163K more than the one predicted by the $k - \epsilon$ model. Contour of the progress variable is showed in Figure 4.9:

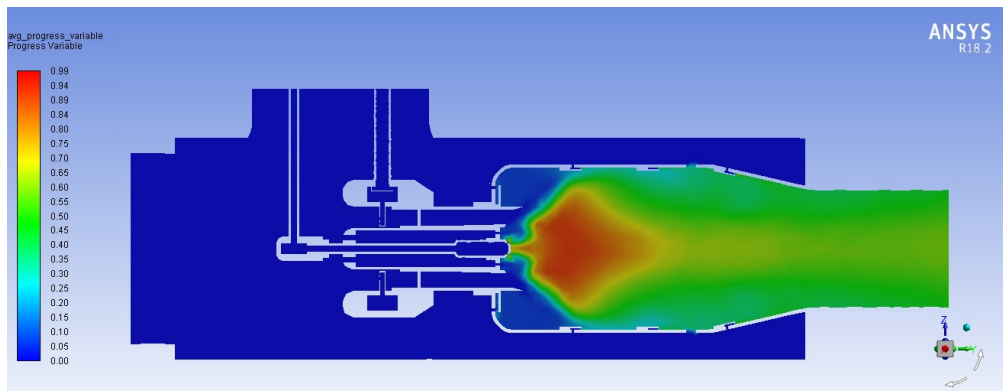
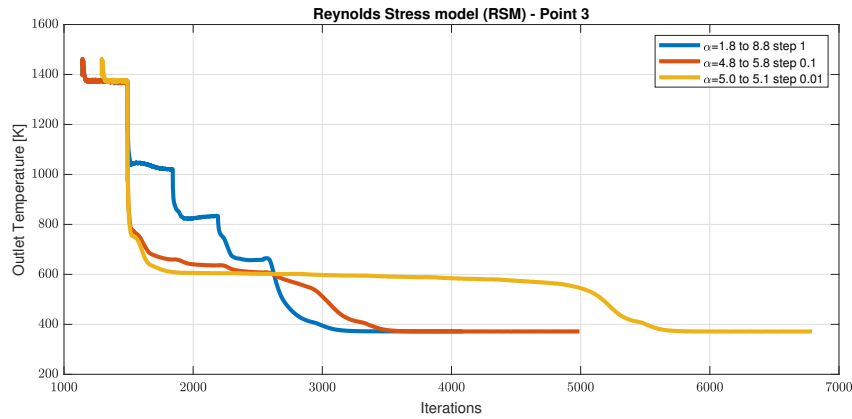
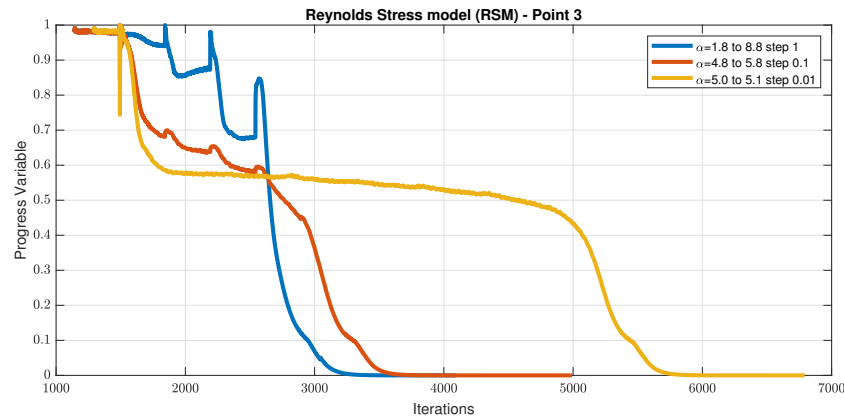


Figure 4.9: Contour of progress variable - $\alpha = 5.05$ - Point 3

It is worth noting that with this turbulence model, just prior to LBO, the progress variable is around 1 in a smaller area of the chamber compared to what predicted the Realizable $k - \epsilon$ model. This is related to the higher temperature contour, the flame resulting from this turbulence model looks to be smaller but with higher temperature, thus its progress variable is around unity only in a smaller region of the chamber. Following, graphs with the outlet temperature and the progress variable are presented and discussed.

(a) *Temperature*(b) *Progress Variable***Figure 4.10:** Temperature and Progress variable evolution during simulation

In Figure 4.10a the monitored outlet temperature is showed during the 3 simulations launched to find LBO for this point. All simulations started from the stable condition of $\alpha = 1.8$ and then fuel mass flow was lowered. The first simulation launched had the coarsest step, 1, and investigated from $\alpha = 1.8$ to 8.8. Blowout was found to occur at $\alpha = 5.8$ so a second simulation was run with a smaller step of 0.1 from 4.8 to 5.8. Here, blowout was found to be at $\alpha = 5.1$ thus a third, last simulation was set up and launched, this time from 5.0 and 5.1 with step 0.01. Looking at the chart, the blowout for this point was declared to be at $\alpha = 5.055$ as a result of the last simulation.

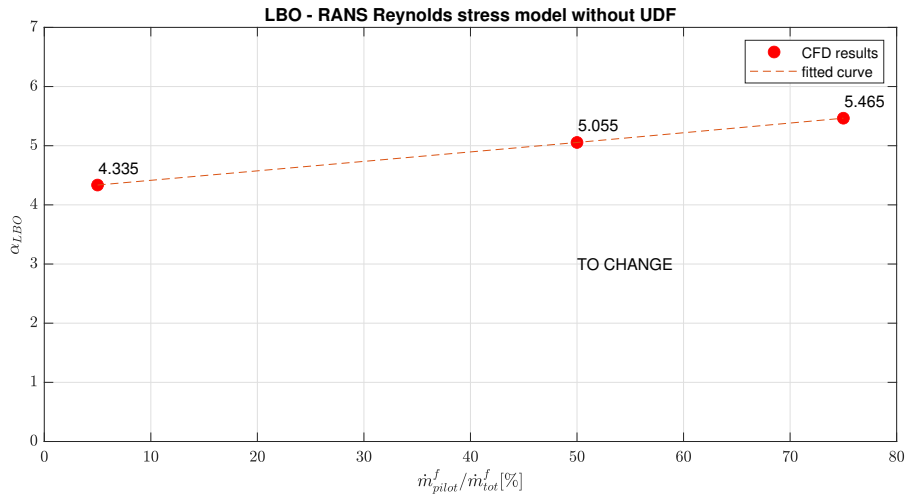


Figure 4.11: Lean Blowout results for Reynolds Stress Model without UDF

As for the Realizable $k - \epsilon$ model without UDF, here the RSM model predicts a greater resistance to lean blowout as mass flow rate from pilot nozzle increases.

4.1.3 Realizable $k - \epsilon$ with UDF

In this section, results gathered with the Realizable $k - \epsilon$ model using User Defined Function for laminar flame speed and critical strain rate are showed. The first case displayed is the one denoted by Point 2, where pilot fuel is 25% of the total fuel injected in the chamber. For this specific point, lean blowout was found to be at $\alpha = 4.555$. The contours at stable combustion where $\alpha = 1.8$ are not showed because they are similar to the $k - \epsilon$ model without UDF. The monitored variables will be displayed right before lean blowout at $\alpha = 4.55$

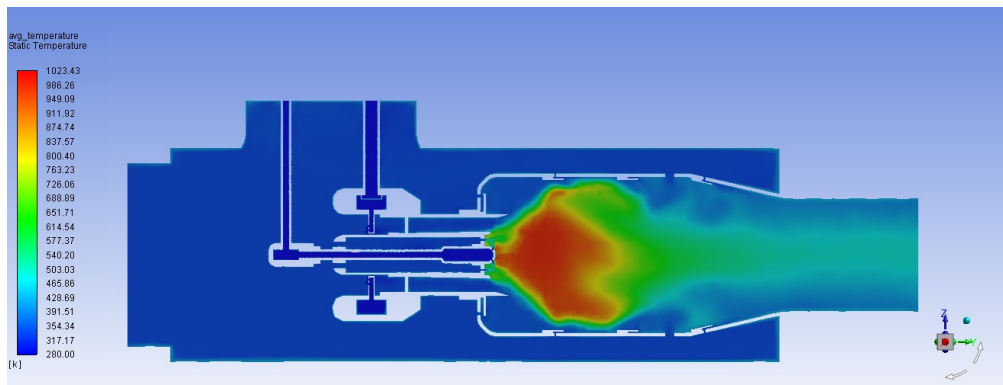


Figure 4.12: Contour of Temperature - $\alpha = 4.55$ - Point 2

The contour of temperature obtained with the UDF is showed in Figure 4.12. Comparing that to the same point for the $k - \epsilon$ model without UDF it is clear how the UDF changed the way the flame is modeled. The modifications of the laminar flame speed and of the critical strain rate deeply modified the contour of temperature. The high temperature region is much bigger than without UDF, but overall the flame has a lower temperature, less than 1000K. The next Figure shows the progress variable in the chamber:

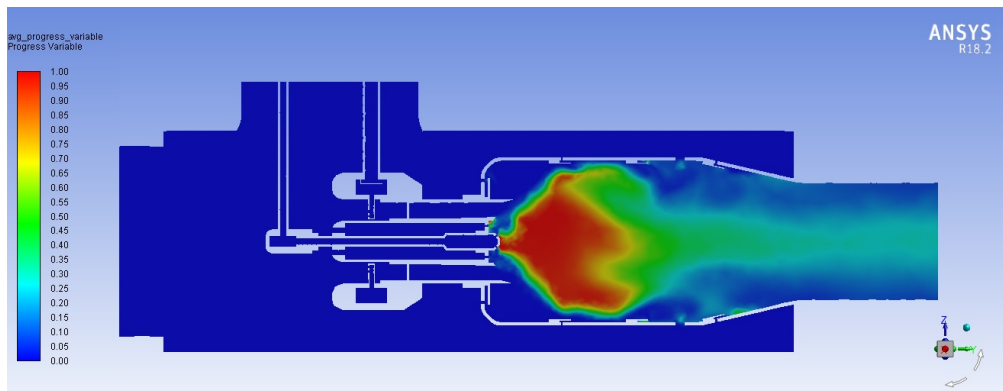
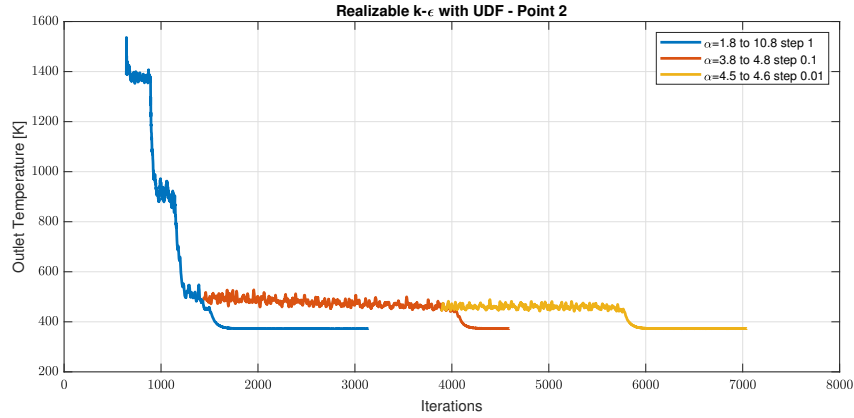
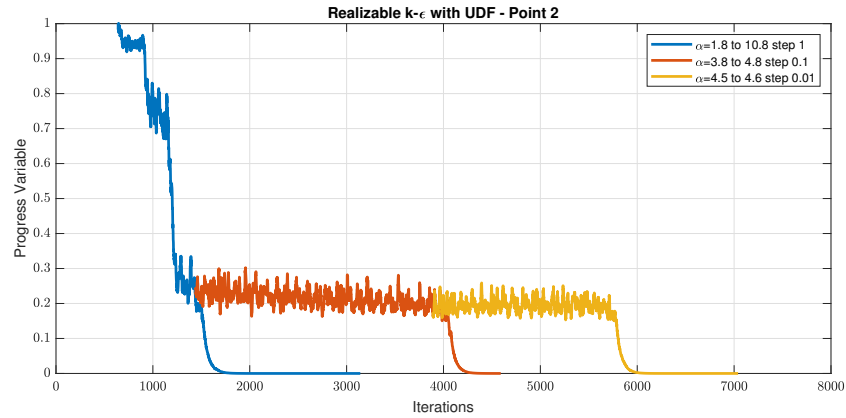


Figure 4.13: Contour of Progress variable - $\alpha = 4.55$ - Point 2

The shape of the progress variable resembles the one of the temperature in Figure 4.12. The zone of burnt products where the progress variable is equal to 1 is completely different from the ones reported without the use of UDF. By looking at this contour, it is clear how the difference in calculating laminar flame speed and the critical strain rate reflects on the shape of the flame. Moreover, it is worth noting how the flame is stretched and irregular as UDF changed the critical strain rate. Without UDF the flame was not so irregular and almost symmetric to the Y-axis. The graphs of the monitored variable are showed below.

(a) *Temperature*(b) *Progress Variable***Figure 4.14:** Temperature and Progress variable evolution during simulation

The first feature of Figure 4.14 worthy of attention is the fact that temperature and progress variable have wide oscillations even at constant fuel mass rate. The good side of this feature is that blowout is more visible, because the drop in temperature and progress variable is more evident compared to the ones without UDF. As for the other turbulence models, three simulation have been launched for this case. The first one from $\alpha = 1.8$ to $\alpha = 10.8$ with step 1. Blowout was found to be at 4.8. the second simulation investigated with a smaller step of 0.1 the conditions between $\alpha = 3.8$ and $\alpha = 4.8$. Here blowout occurred at 4.6 so a third, last simulation was launched from $\alpha = 4.5$ to $\alpha = 4.6$. Blowout was declared to be at $\alpha = 4.555$ as a

result of the last simulation.

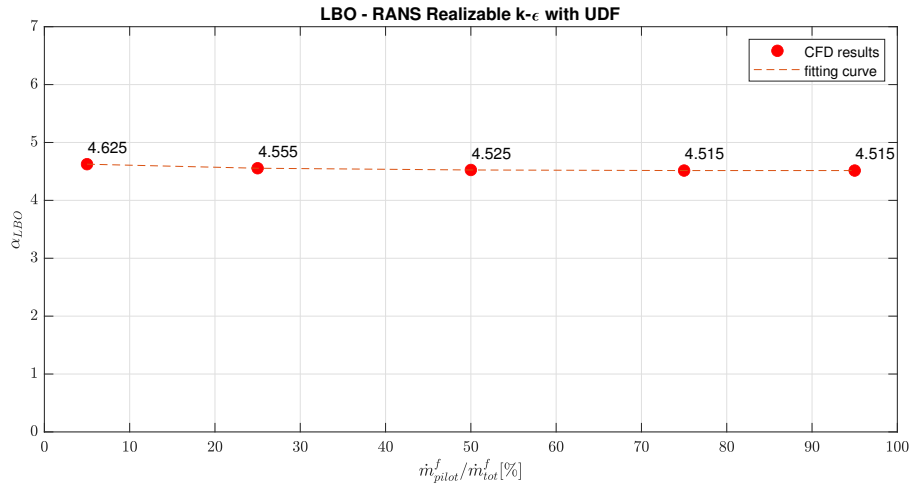


Figure 4.15: Lean Blowout results for Realizable $k - \epsilon$ model with UDF

The results for the Realizable $k - \epsilon$ model with UDF shows an overall slightly decreasing resistance to lean blowout as the mass flow rate of the pilot fuel increases. This behaviour is very different compared to the ones of the models without UDF, as they reported a much clear tendency to increase blowout resistance as the pilot fuel increases.

Following, the contours of progress variable and static temperature for **premixed flamelets**:

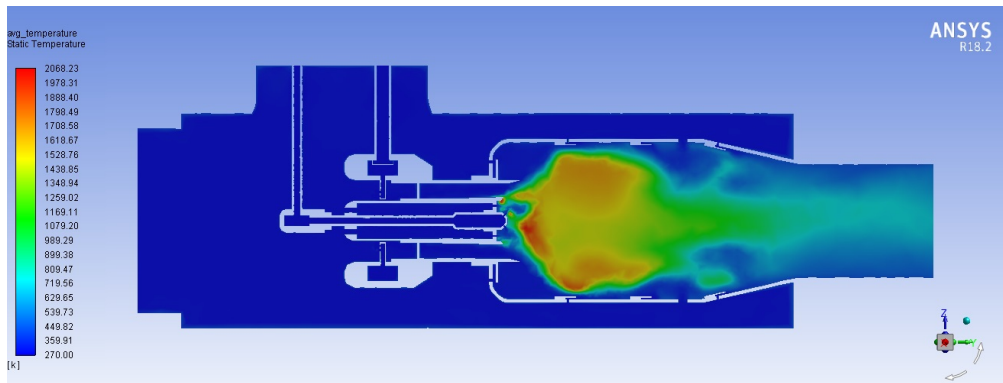


Figure 4.16: Contour of Temperature - $\alpha = 2.85$ - Point 2

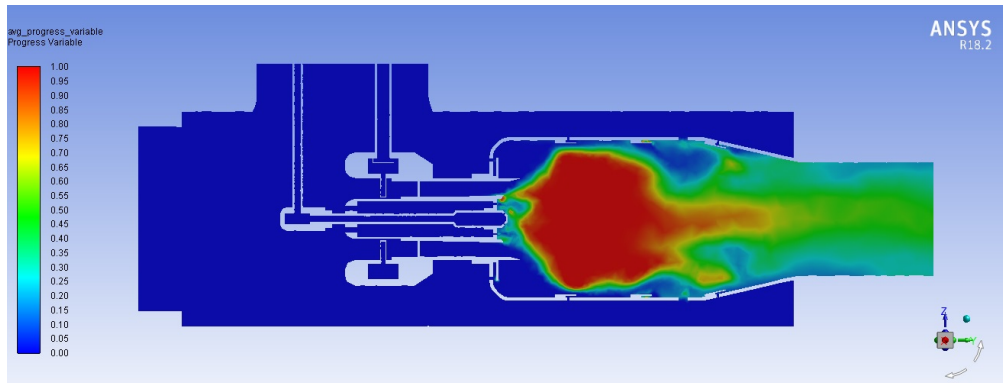


Figure 4.17: Contour of Progress variable - $\alpha = 2.85$ - Point 2

The contour of temperature showed in Figure (4.16) is a little different from the one computed with diffusive flamelets in Figure (4.12). The region where the flame is developed is larger and the flame appears to be more turbulent, with a smaller region of high temperature. The different dimensions of the flame are clear from the contour of the progress variable in Figure (4.17). Here, it is clear how most of the reactions take place in the recirculation zone, as the progress variable is equal to 1 in a wide region of the combustor.

4.1.4 URANS

In this section, results gathered with URANS equations are showed. The turbulence model used is the Realizable $k - \epsilon$. The first case showed is the one named as Point 2, where pilot fuel is 25% of the total fuel. For this specific point, lean blowout was found to be at $\alpha = 4.255$. The contours of temperature, velocity and progress variable at stable combustion where $\alpha = 1.8$ are not showed since they're similar to the ones showed and discussed in section 4.1.1. The following contours shows the monitored variable just prior to lean blowout, at $\alpha = 4.25$:

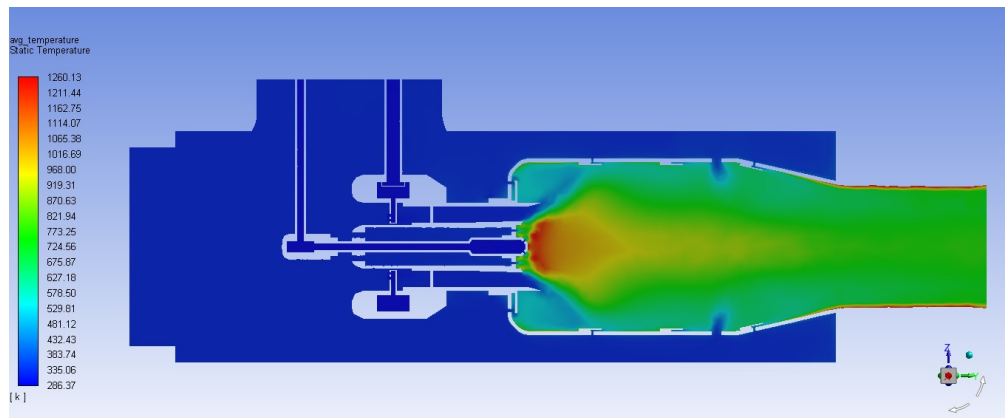


Figure 4.18: Contour of Temperature - $\alpha = 4.25$ - Point 2

The contour of temperature just prior to lean blowout using URANS is different from the ones showed earlier. The flame looks to be very close to the nozzles, and with a small area compared to the other turbulence models. The temperature range reached by the flame is slightly higher than the ones reached by the other turbulence models. Following, the contour of the progress variable is showed.

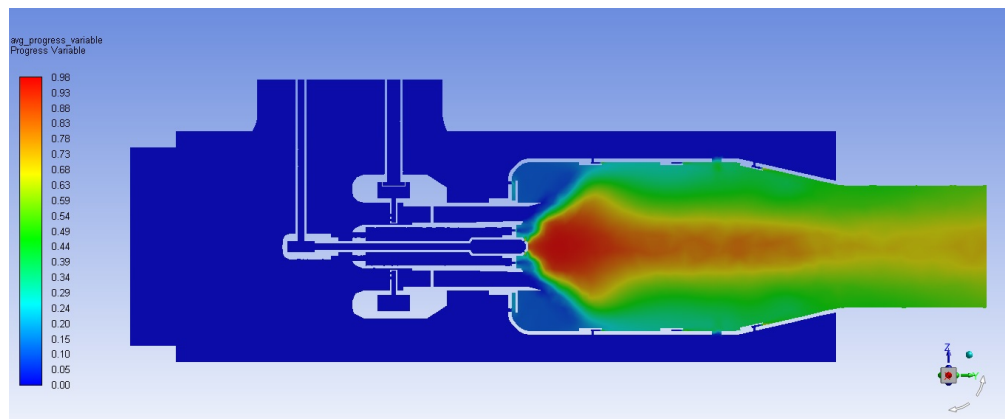
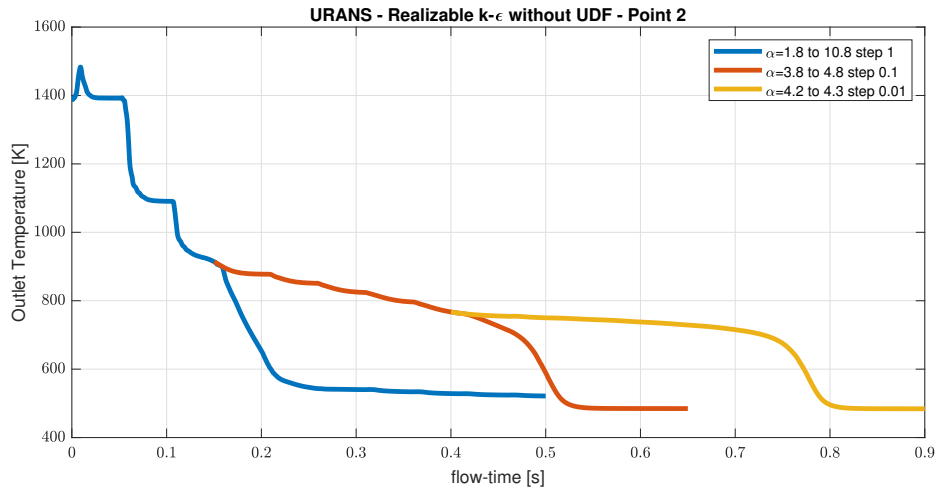
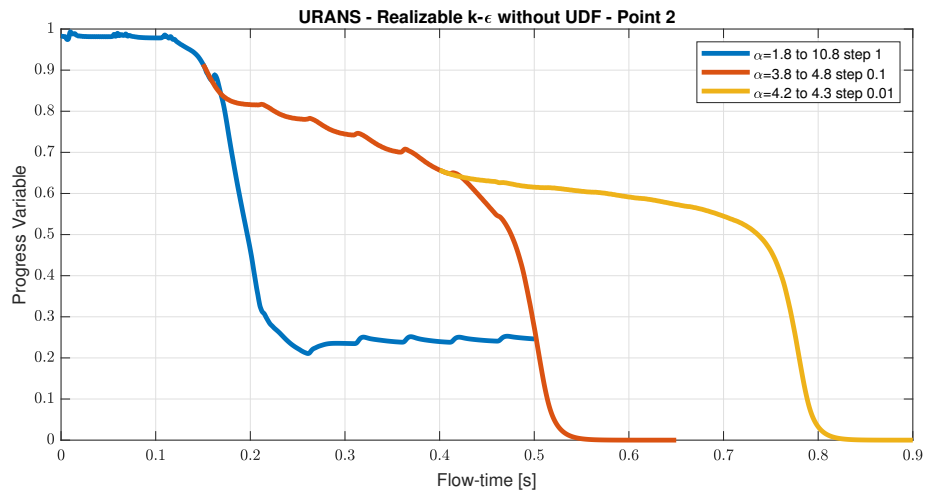


Figure 4.19: Contour of Progress variable - $\alpha = 4.25$ - Point 2

The contour of the progress variable is showed in Figure 4.19. Its shape is very similar to the one in Figure 4.5b where the same turbulence model was used but for steady solutions. The graphs for the monitored variable are showed below.



(a) Temperature



(b) Progress Variable

Figure 4.20: Temperature and Progress variable evolution during simulation

As in all model without using UDF, the decay of temperature and the progress variable is slow.

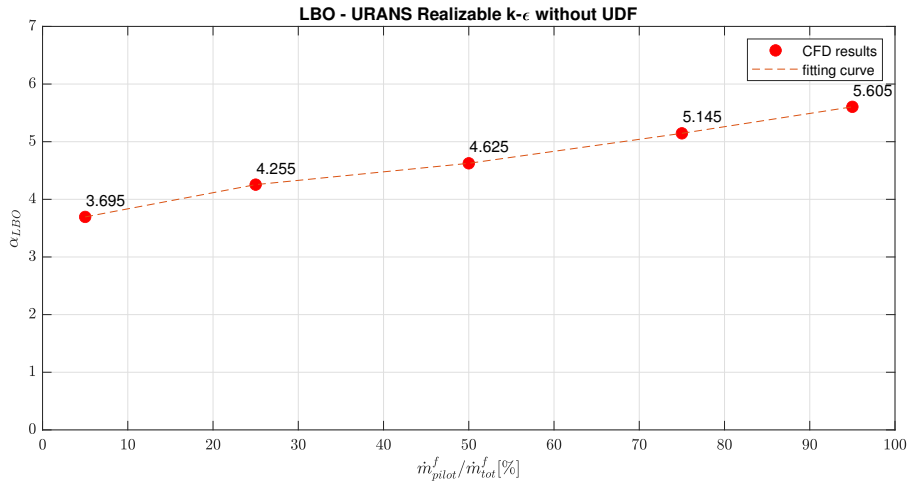


Figure 4.21: Lean Blowout results for URANS Realizable $k - \epsilon$ model without UDF

As for the other turbulence models, the URANS with the Realizable $k - \epsilon$ model predicted a growing resistance to lean blowout as the fuel mass flow rate of the pilot increases.

4.2 Experimental results

Experimental measures were taken in the Samara National Research University with a reference burner showed in section 3.6. The gathered data were interpolated using MATLAB, employing a linear interpolation. The black curve showed in Figure 4.22 and Figure 4.23 is the result of the interpolation. The first graph to be shown is the one with diffusive flamelets.

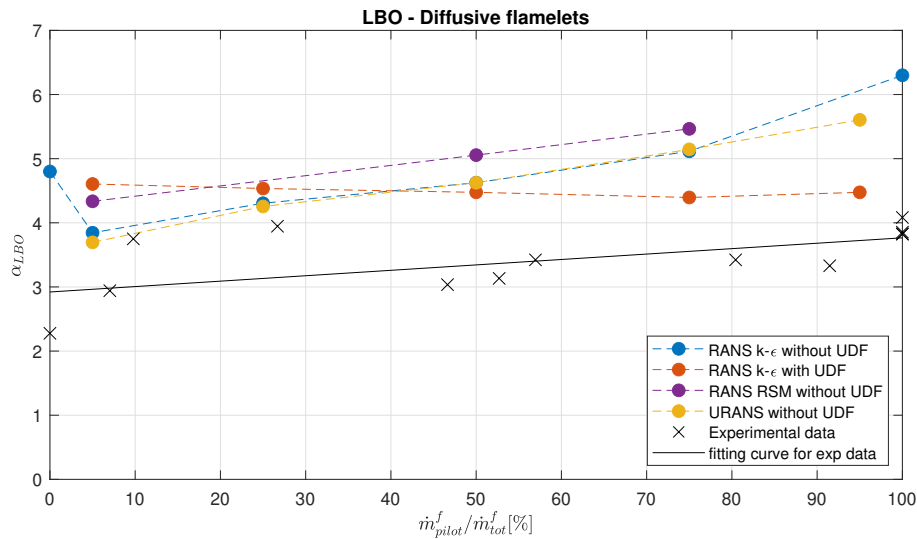


Figure 4.22: Comparison with experimental data - Diffusive Flamelets

In Figure 4.22, numerical prediction with diffusive flamelets are compared with experimental data. As clear from the picture, results from all the turbulence models differ from the experimental results, especially in the region where mass flow rate from pilot fuel is predominant. In all cases, LBO predictions overestimates the experimental value. The Realizable $k - \epsilon$ model with UDF has the most accurate prediction among all other, but its relative error goes from around 8% when $\frac{\dot{m}_{pilot}^f}{\dot{m}_{tot}^f} = 25\%$ to a peak of 30% when pilot and main nozzles have the same mass flow rate. The results for the premixed flamelets are shown below.

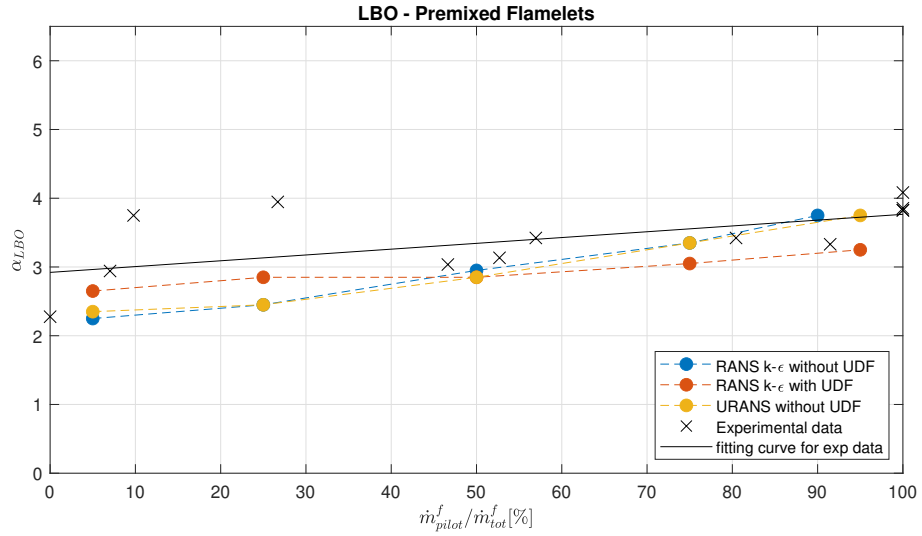


Figure 4.23: Comparison with experimental data - Premixed Flamelets

In Figure 4.23 the numerical results obtained with premixed flamelets are compared to experimental data. The agreement with the latter is much better than with diffusive flamelet. The relative error is in fact minor than 10% among all studied cases of different pilot and main fuel mass flow rate when using UDF. The different modelization of the laminar flame speed and the critical strain rate seems to have a small influence to the results, but overall the predictions with UDF are better than without UDF. These predictions are acceptable as premixed flamelets predicts better chemistry-turbulence interaction of the flow in the primary zone.

Chapter 5

Conclusions

As a result of computational and experimental studies, lean blowout for a small gas turbine engine's combustor with pilot flame was studied. The influence on lean blowout of different turbulence models was investigated, and some user-defined functions were used to model flame quenching closer to reality. As a result of the study, when using diffusive flamelets, all turbulence models appear to overestimate LBO prediction when diffusive pilot flame is predominant. The numerical prediction is accurate when the mass flow rate of the pilot fuel is lower, reaching a relative error of around 8% when $\frac{\dot{m}_{pilot}^f}{\dot{m}_{tot}^f} = 25\%$. As pilot fuel mass flow rate increases, the numerical prediction gets less accurate, reaching a relative error of around 30%. The use of UDF with the Realizable $k - \epsilon$ model gets the best accuracy through the whole range of fuel distribution, when using diffusive flamelets. However, changing the type of flamelets to premixed made the numerical prediction much closer to experimental results. Chemistry-turbulence interaction appears to be simulated better from Premixed flamelets which can properly capture the interaction between diffusive flame from pilot fuel and the premixed flame from main fuel. Here, the use of UDF seems to have a small influence of blowout prediction, but demonstrated to model the flame closer to reality. In fact, the flame appears to be much stretched and turbulent compared to the case without UDF. The relative error is below

10% among all studied cases with premixed flamelets, which resulted in a good agreement with the experimental data. Validation for this models needs however further investigations, as it should be tested for a wide range of boundary conditions, but RANS capabilities to simulate Lean Blowout with relative low computational costs have been demonstrated to be reliable for this operating condition.

5.1 Future developments

This study has promising possible developments. The use of finer meshes with smaller elements can be investigated. Moreover, having found lean blowout in a certain range with RANS models, it is a good starting point for a possible LES analysis. As explained thoroughly in the first chapter, LES have been widely validated for studying complex and unsteady phenomena as lean blowout. Because of the high computational cost of LES analysis, beginning from what was found in this work is a good outset. The influence of different fuels as alternative ones on lean blowout can be investigated too.

Appendix A

Appendix

The input file for the Supercomputer "Sergey Korolev" installed at the Supercomputing Center of the Samara University is reported below:

Fluent_input

```
1 file/read-case-data Point2alpha1.8_combustion_start.cas.gz
2
3 /define/user-defined/compiled-functions load "libudf"
4
5 /solve/iterate 250
6 /file/write-case-data Point2alpha1.8_250it.cas.gz
7 /define/boundary-conditions/mass-flow-inlet fuel_pilot yes yes no
   0.1032 no 288 no 0 no yes no no yes 5 10 no 0 no 0 no 1 no 0
8 /define/boundary-conditions/mass-flow-inlet fuel_main yes yes no
   0.3097 no 288 no 0 no yes no no yes 5 10 no 0 no 0 no 1 no 0
9 /solve/iterate 250
10 /file/write-case-data Point2alpha2.8_250it.cas.gz
11 /define/boundary-conditions/mass-flow-inlet fuel_pilot yes yes no
   0.0761 no 288 no 0 no yes no no yes 5 10 no 0 no 0 no 1 no 0
12 /define/boundary-conditions/mass-flow-inlet fuel_main yes yes no
   0.2282 no 288 no 0 no yes no no yes 5 10 no 0 no 0 no 1 no 0
13 /solve/iterate 250
14 /file/write-case-data Point2alpha3.8_250it.cas.gz
```

```
15 /define/boundary-conditions/mass-flow-inlet fuel_pilot yes yes no
    0.0602 no 288 no 0 no yes no no yes 5 10 no 0 no 0 no 1 no 0
16 /define/boundary-conditions/mass-flow-inlet fuel_main yes yes no
    0.1806 no 288 no 0 no yes no no yes 5 10 no 0 no 0 no 1 no 0
17 /solve/iterate 250
18 /file/write-case-data Point2alpha4.8_250it.cas.gz
19 /define/boundary-conditions/mass-flow-inlet fuel_pilot yes yes no
    0.0498 no 288 no 0 no yes no no yes 5 10 no 0 no 0 no 1 no 0
20 /define/boundary-conditions/mass-flow-inlet fuel_main yes yes no
    0.1495 no 288 no 0 no yes no no yes 5 10 no 0 no 0 no 1 no 0
21 /solve/iterate 250
22 /file/write-case-data Point2alpha5.8_250it.cas.gz
23 /define/boundary-conditions/mass-flow-inlet fuel_pilot yes yes no
    0.0425 no 288 no 0 no yes no no yes 5 10 no 0 no 0 no 1 no 0
24 /define/boundary-conditions/mass-flow-inlet fuel_main yes yes no
    0.1275 no 288 no 0 no yes no no yes 5 10 no 0 no 0 no 1 no 0
25 /solve/iterate 250
26 /file/write-case-data Point2alpha6.8_250it.cas.gz
27 /define/boundary-conditions/mass-flow-inlet fuel_pilot yes yes no
    0.0371 no 288 no 0 no yes no no yes 5 10 no 0 no 0 no 1 no 0
28 /define/boundary-conditions/mass-flow-inlet fuel_main yes yes no
    0.1112 no 288 no 0 no yes no no yes 5 10 no 0 no 0 no 1 no 0
29 /solve/iterate 250
30 /file/write-case-data Point2alpha7.8_250it.cas.gz
31 /define/boundary-conditions/mass-flow-inlet fuel_pilot yes yes no
    0.0328 no 288 no 0 no yes no no yes 5 10 no 0 no 0 no 1 no 0
32 /define/boundary-conditions/mass-flow-inlet fuel_main yes yes no
    0.0985 no 288 no 0 no yes no no yes 5 10 no 0 no 0 no 1 no 0
33 /solve/iterate 250
34 /file/write-case-data Point2alpha8.8_250it.cas.gz
35 /define/boundary-conditions/mass-flow-inlet fuel_pilot yes yes no
    0.0295 no 288 no 0 no yes no no yes 5 10 no 0 no 0 no 1 no 0
36 /define/boundary-conditions/mass-flow-inlet fuel_main yes yes no
    0.0885 no 288 no 0 no yes no no yes 5 10 no 0 no 0 no 1 no 0
37 /solve/iterate 250
```

Appendix

```
38 /file/write-case-data Point2alpha9.8_250it.cas.gz
39 /define/boundary-conditions/mass-flow-inlet fuel_pilot yes yes no
    0.0268 no 288 no 0 no yes no no yes 5 10 no 0 no 0 no 1 no 0
40 /define/boundary-conditions/mass-flow-inlet fuel_main yes yes no
    0.0803 no 288 no 0 no yes no no yes 5 10 no 0 no 0 no 1 no 0
41 /solve/iterate 250
42 /file/write-case-data Point2alpha10.8_250it.cas.gz
43
44 exit yes
```

Bibliography

- [1] *2030 climate & energy framework*. Text. URL: https://ec.europa.eu/clima/policies/strategies/2030_en (visited on 12/20/2020) (cit. on p. 1).
- [2] *Nitrogen oxides (NO_x) emissions — European Environment Agency*. URL: <https://www.eea.europa.eu/data-and-maps/indicators/eea-32-nitrogen-oxides-nox-emissions-1/assessment.2010-08-19.0140149032-3> (visited on 12/20/2020) (cit. on p. 2).
- [3] A. H. Lefebvre. «Fuel Effects on Gas Turbine Combustion—Ignition, Stability, and Combustion Efficiency». In: *Journal of Engineering for Gas Turbines and Power* 107.1 (Jan. 1985), pp. 24–37 (cit. on pp. 3, 4).
- [4] Zhonghao Wang, Bin Hu, Qingjun Zhao, and Jianzhong Xu. «Towards Predicting Lean Blow-Off Based on Damkohler Number and Practical Reaction Zone». In: (2017), p. 11 (cit. on p. 3).
- [5] Fa Xie, Yong Huang, Bin Hu, and Fang Wang. «Improved Semiempirical Correlation to Predict Lean Blowout Limits for Gas Turbine Combustors». In: *Journal of Propulsion and Power* 28 (Jan. 2012), pp. 197–203 (cit. on p. 5).
- [6] Bin Hu, Qingjun Zhao, and Jianzhong Xu. «Predicting Lean Blowout Limit of Combustors Based on Semi-Empirical Correlation and Simulation». In: *Journal of Propulsion and Power* 32 (Aug. 2015), pp. 1–13 (cit. on p. 5).

- [7] Saad Akhtar. «Numerical investigation of flame structure and blowout limit for lean premixed turbulent methane-air flames under high pressure conditions». In: *Applied Energy* (2018), p. 12 (cit. on pp. 5, 7, 35).
- [8] Joshua Piehl, Luis Bravo, Waldo Acosta, Gaurav Kumar, Scott Drennan, and Omid Samimi-Abianeh. «On Predictions of Fuel Effects on Lean Blow Off Limits in a Realistic Gas Turbine Combustor Using Finite Rate Chemistry». In: *Volume 4B: Combustion, Fuels, and Emissions*. American Society of Mechanical Engineers, June 2018 (cit. on pp. 5–7).
- [9] L. Esclapez, P. C. Ma, and M. Ihme. «Large-eddy simulation of fuel effect on lean blow-out in gas turbines». In: Center for Turbulence Research Annual Research Briefs (2015) (cit. on pp. 6, 7).
- [10] Peter C. Ma, Hao Wu, Jeffrey W. Labahn, Thomas Jaravel, and Matthias Ihme. «Analysis of transient blow-out dynamics in a swirl-stabilized combustor using large-eddy simulations». In: *Proceedings of the Combustion Institute* 37.4 (2019), pp. 5073–5082 (cit. on pp. 6, 7).
- [11] Zhibo Zhang, Hongtao Zheng, Zhiming Li, Yajun Li, Gang Pan, and Xi Chen. «A New Method for Numerical Prediction of Lean Blowout in Aero-Engine Combustor». In: *ASME 2013 Power Conference*. Volume 1: Fuels et al., 2013 (cit. on p. 7).
- [12] Zhonghao Wang, Bin Hu, Qingjun Zhao, and Jianzhong Xu. «Towards Predicting Lean Blow-Off Based on Damköhler Number and Practical Reaction Zone». In: *Volume 4A: Combustion, Fuels and Emissions*. June 2017 (cit. on p. 7).
- [13] Mohammad Soroudi, Sajed Hadi Bafekr, Mehdi Timaji, and N Rasooli. «A Priori Calculation of Lean Blowout Limit in an Industrial Gas Turbine Combustor». In: Jan. 2013 (cit. on p. 8).

- [14] Bin Hu, Yong Huang, and Jianzhong Xu. «A Hybrid Semi-empirical Model for Lean Blow-Out Limit Predictions of Aero-engine Combustors». In: *Journal of Engineering for Gas Turbines and Power* 137.3 (Mar. 2015). ISSN: 0742-4795 (cit. on p. 8).
- [15] M. Tabatabaian. *CFD Module: Turbulent Flow Modeling*. Multiphysics Modeling Series. Mercury Learning and Information, 2015 (cit. on p. 11).
- [16] Uriel Frisch. *Turbulence: The Legacy of A.N. Kolmogorov*. Nov. 1995 (cit. on p. 12).
- [17] Yang Zhiyin. «Large-eddy simulation: Past, present and the future». In: *Chinese Journal of Aeronautics* 28.1 (2015), pp. 11–24 (cit. on p. 12).
- [18] Versteeg Henk Kaarle. *An introduction to computational fluid dynamics : the finite volume method / H.K. Versteeg and W. Malalasekera*. Second edition. Pearson Education Ltd. (cit. on p. 12).
- [19] Jiyuan Tu, Guan-Heng Yeoh, and Chaoqun Liu. «Chapter 3 - Governing Equations for CFD: Fundamentals». In: *Computational Fluid Dynamics (Third Edition)*. Third Edition. Butterworth-Heinemann, 2018, pp. 65–124 (cit. on p. 14).
- [20] C. Mayes, H. Schlichting, E. Krause, H.J. Oertel, and K. Gersten. *Boundary-Layer Theory*. Physic and astronomy. Springer Berlin Heidelberg, 2003 (cit. on p. 14).
- [21] Guido Buresti. «A note on Stokes' hypothesis». In: *Acta Mechanica* 226 (Oct. 2015) (cit. on p. 17).
- [22] F. Moukalled, L. Mangani, and M. Darwish. *The Finite Volume Method in Computational Fluid Dynamics: An Advanced Introduction with OpenFOAM and Matlab*. 1st. Springer, 2015 (cit. on p. 17).
- [23] R. J. Kee, Michael Elliott Coltrin, Peter Glarborg, and Huayang Zhu. *Chemically Reacting Flow: Theory, Modeling, and Simulation*. John Wiley & Sons, 2017 (cit. on p. 19).

- [24] «2 - Field Modeling Approach». In: *Computational Fluid Dynamics in Fire Engineering*. Ed. by Guan Heng Yeoh and Kwok Kit Yuen. Burlington: Butterworth-Heinemann, 2009, pp. 29–133 (cit. on p. 21).
- [25] Joel H. Ferziger and Milovan Peric. *Computational Methods for Fluid Dynamics*. Springer Berlin Heidelberg, Nov. 2001 (cit. on pp. 21, 22, 33, 34).
- [26] J. Boussinesq. *Essai sur la théorie des eaux courantes*. Mémoires présentés par divers savants à l'Académie des Sciences XXIII, 1877 (cit. on p. 23).
- [27] L. Prandtl. «7. Bericht über Untersuchungen zur ausgebildeten Turbulenz». In: *ZAMM - Journal of Applied Mathematics and Mechanics / Zeitschrift für Angewandte Mathematik und Mechanik* 5.2 (1925), pp. 136–139 (cit. on p. 23).
- [28] W.P. Jones and Brian Launder. «The Prediction of Laminarization with a Two-Equation Model of Turbulence, "» in: *Intj. Heat Mass Transfer* 5 (Jan. 1973), pp. 301–314 (cit. on pp. 24, 25).
- [29] David C. Wilcox. *Turbulence Modeling for CFD*. DCW Industries, Incorporated, 1994 (cit. on p. 24).
- [30] Brian Launder and D.B. Spalding. «The numerical computation of turbulent flows». In: *Comput. Methods Appl. Mech. Eng.* 103 (Jan. 1974), pp. 456–460 (cit. on p. 25).
- [31] Tsan-Hsing Shih, William W. Liou, Aamir Shabbir, Zhigang Yang, and Jiang Zhu. «A new k-e eddy viscosity model for high reynolds number turbulent flows». In: *Computers & Fluids* 24.3 (Mar. 1995), pp. 227–238 (cit. on pp. 26–28).
- [32] W. C. Reynolds. *Fundamentals of Turbulence for Turbulence Modeling and Simulation*. 1987 (cit. on p. 27).
- [33] T. Shih, J. Zhu, and J. Lumley. «A new Reynolds stress algebraic equation model». In: (1994) (cit. on p. 27).

- [34] Brian Launder, G. Reece, and W. Rodi. «Progress in the Development of a Reynolds Stress Turbulence Closure». In: *Journal of Fluid Mechanics* 68 (Apr. 1975), pp. 537–566 (cit. on p. 29).
- [35] Brian E. Launder. «Second-moment closure: present... and future?» In: *International Journal of Heat and Fluid Flow* 10.4 (Dec. 1989), pp. 282–300 (cit. on p. 29).
- [36] Bart J. Daly and Francis H. Harlow. «Transport Equations in Turbulence». In: *The Physics of Fluids* 13.11 (Nov. 1970), pp. 2634–2649 (cit. on p. 30).
- [37] F. S. Lien and M. A. Leschziner. «Assessment of turbulence-transport models including non-linear rng eddy-viscosity formulation and second-moment closure for flow over a backward-facing step». In: *Computers & Fluids* 23.8 (Nov. 1994), pp. 983–1004 (cit. on p. 30).
- [38] M. Gibson and Brian Launder. «Ground Effects on Pressure Fluctuations in the Atmospheric Boundary Layer». In: *Journal of Fluid Mechanics* 86 (June 1978), pp. 491–511 (cit. on p. 31).
- [39] S. Sarkar and L. Balakrishnan. «Application of a Reynolds Stress Turbulence Model to the Compressible Shear Layer». In: *ICASE Report 90-18 NASA CR 182002* (1990) (cit. on p. 32).
- [40] R. Henkes, F. F. V. D. Vlugt, and C. J. Hoogendoorn. «Natural-convection flow in a square cavity calculated with low-Reynolds-number turbulence models». In: (1991) (cit. on p. 32).
- [41] S. H. Lam and D. A. Coussis. «Conventional asymptotics and computational singular perturbation for simplified kinetics modelling». In: *Reduced Kinetic Mechanisms and Asymptotic Approximations for Methane-Air Flames: A Topical Volume*. Ed. by Mitchell D. Smooke. Springer, 1991 (cit. on p. 34).
- [42] U. Maas and S. B. Pope. «Simplifying chemical kinetics: Intrinsic low-dimensional manifolds in composition space». In: *Combustion and Flame* 88.3 (1992) (cit. on p. 35).

- [43] Arthur Jan Fijałkowski. *Polski: Różne kolory i kształty płomienia palnika Bunsena w zależności od ilości wpuszczanego powietrza*. URL: https://commons.wikimedia.org/wiki/File:Bunsen_burner_flame_types.jpg (cit. on p. 36).
- [44] J. A. Van Oijen and L. P. H. De Goey. «Modelling of Premixed Laminar Flames using Flamelet-Generated Manifolds». In: *Combustion Science and Technology* 161.1 (Dec. 2000), pp. 113–137 (cit. on p. 36).
- [45] N. Peters. «Laminar diffusion flamelet models in non-premixed turbulent combustion». In: *Prog. Energy Combust. Sci.* 10 (1984) (cit. on p. 37).
- [46] Seyed Hossein Jamali, Likun Ma, and D. Roekaerts. «Computational Study of Ethanol Flameless Combustion Using FGM and Steady Flamelet». In: *9th Mediterranean Combustion Symposium*. 2015 (cit. on pp. 37, 38).
- [47] Ken Bray, Pascale Domingo, and Luc Vervisch. «Role of the progress variable in models for partially premixed turbulent combustion». In: *Combustion and Flame* 141 (), pp. 431–437 (cit. on p. 39).
- [48] ANSYS Inc. *ANSYS Fluent Theory Guide*. Version 18.2.0. 2017 (cit. on pp. 39, 40).
- [49] Ali Cemal Benim and Khawar J. Syed. «Chapter 2 - Concepts Related to Combustion and Flow in Premix Burners». In: *Flashback Mechanisms in Lean Premixed Gas Turbine Combustion*. Boston: Academic Press, 2015, pp. 5–18 (cit. on p. 41).
- [50] Kenneth Kuan-yun Kuo and Ragini Acharya. *Fundamentals of Turbulent and Multiphase Combustion*. John Wiley & Sons, 2012 (cit. on p. 42).
- [51] J. Göttgens, F. Mauss, and N. Peters. «Analytic approximations of burning velocities and flame thicknesses of lean hydrogen, methane, ethylene, ethane, acetylene, and propane flames». In: vol. 24. 1. 1992, pp. 129–135 (cit. on pp. 42, 43).

- [52] Mohamad Metghalchi and James C. Keck. «Burning velocities of mixtures of air with methanol, isooctane, and indolene at high pressure and temperature». In: *Combustion and Flame* 48 (1982), pp. 191–210 (cit. on p. 43).
- [53] S. Lukachev, Sergei Matveev, Ivan Zubrilin, and A. Sigidaev. «Dependence of methane laminar flame propagation speed on the pressure and initial temperature». In: *VESTNIK of Samara University. Aerospace and Mechanical Engineering* 15 (2017), p. 224 (cit. on pp. 43, 47).
- [54] V. Zimont, Wolfgang Polifke, Marco Bettelini, and Wolfgang Weisenstein. «An Efficient Computational Model for Premixed Turbulent Combustion at High Reynolds Numbers Based on a Turbulent Flame Speed Closure». In: *Journal of Engineering for Gas Turbines and Power-transactions of The Asme* 120 (1998) (cit. on pp. 47, 48).
- [55] *Supercomputer Sergei Korolev / Supercomputer Center of Samara University*. URL: <http://hpc.ssau.ru/node/6> (cit. on p. 59).